



# Shallow Composition and Structure of the Upper Part of the Exhumed San Gabriel Fault, California: Implications for Fault Processes

Kaitlyn Crouch <sup>\*1,2</sup>, James P. Evans <sup>1</sup>

<sup>1</sup>Department of Geosciences, Utah State University, Logan, UT, USA | <sup>2</sup>Now at Department of Geosciences, University of Wisconsin, Madison, WI, USA

**Abstract** Quantifying shallow fault zone structure and characteristics is critical for accurately modeling the complex mechanical behavior of earthquakes as energy moves within faults from depth. We examine macro- to microstructures, mineralogy, and properties from drill core analyses of fault-related rocks in the steeply plunging ALT-B2 geotechnical borehole (total depth of 493 m) across the San Gabriel Fault zone, California. We use macroscopic drill core and outcrop-sample analyses, core-based damage estimates, optical microscopy, and X-ray diffraction mineralogic analyses to determine the fault zone structure, deformation mechanisms, and alteration patterns of exhumed deformed rocks formed in a section of the fault that slipped 5–12 million years ago, with evidence for some Quaternary slip. The fault consists of two principal slip zones composed of cohesive cataclasite, ultracataclasite, and intact clay-rich, highly foliated gouge within upper and lower damage zones ~60 m and 50 m thick. The upper ~6.5 m thick principal slip zone separates Mendenhall Gneiss and Josephine Granodiorite, and a lower 11 m thick principal slip is enclosed within the Josephine Granodiorite. Microstructures record overprinted brittle fractures, cohesive cataclasites, veins, sheared clay-rich rocks, and folded foliated and carbonate-rich horizons in the damage zones. Carbonate veins are common in the lower fault zone, and alteration and mineralization assemblages consist of clays, epidote, calcite, zeolites, and chloritic minerals. These data show that shallow portions of the fault experienced fluid-rock interactions that led to alteration, mineralization, and brittle and semi-brittle deformation that led to the formation of damage zones and narrow principal slip zones that are continuous down-dip and along strike.

Executive Editor:  
**Janine Kavanagh**  
Associate Editors:  
**Jack Williams**  
Technical Editor:  
**Wan-Lin Hu**

Reviewers:  
**Benjamin Melosh**  
**Anonymous 1**  
**Anonymous 2**

Submitted:  
**8 December 2022**  
Accepted:  
**8 August 2023**  
Published:  
**25 September 2023**

## 1 Introduction

The shallow part of faults, defined here as the top of faulted bedrock to depths of ~2–3 km (Figure 1), is a transitional zone where fault slip and energy are distributed from seismogenic depths to the Earth's surface (Figure 1). Inversions of a range of data sets indicate that the maximum values of coseismic slip on faults are typically found at depths > 3 km (Marone and Saffer, 2007; Kaneko and Fialko, 2011; Dolan and Haravitch, 2014; Scott et al., 2019), as are the depths of on-fault hypocenters in densely instrumented parts of Southern California (Hauksson and Meier, 2019). Mechanisms invoked to explain on-fault slip deficits on the shallowest parts of faults include fault-zone plastic or inelastic deformation (Roten et al., 2017a; Scott et al., 2019), off-fault distributed deformation not included in inversion schemes (Scott et al., 2019; Marchandon et al., 2021), and fault creep (Chen and Bürgmann, 2017; Marchandon et al., 2021). Marchandon et al. (2021) suggest that some slip deficits are artifacts of inversion schemes that do not capture all the deformation across fault zones.

Determining the composition, microstructures, and properties of fault-related rocks in the shallow parts of fault zones is critical to modeling how seismic energy and slip are distributed from earthquake foci to the earth's surface (Boulton et al., 2017; Nevitt et al., 2020; Marchandon et al., 2021). The range of dominant deformation mechanisms and fault-related rock compositions, determined from microstructural, mineralogic, and geochemical studies, indicates that the uppermost regions of faults consist of gouge and breccia, which give way to cataclasites at 2–3 km (Figure 1A). These observations suggest that frictional, and thus seismic, behavior is dominated by stable sliding and lack of earthquake nucleation (Figure 1).

Continuous drill core and related borehole log data acquired across fault zones provide critical data that can be used to help determine the processes in fault zones in the upper several km of the Earth's crust (Ohtani et al., 2000; Song et al., 2007; Zoback et al., 2010; Boullier, 2011; Sutherland et al., 2012; Bradbury et al., 2015; Duan et al., 2016). Cored sections of faults provide rocks, fluid samples, and borehole-based geophysical data that are

\*✉ [kcrouch2@wisc.edu](mailto:kcrouch2@wisc.edu)

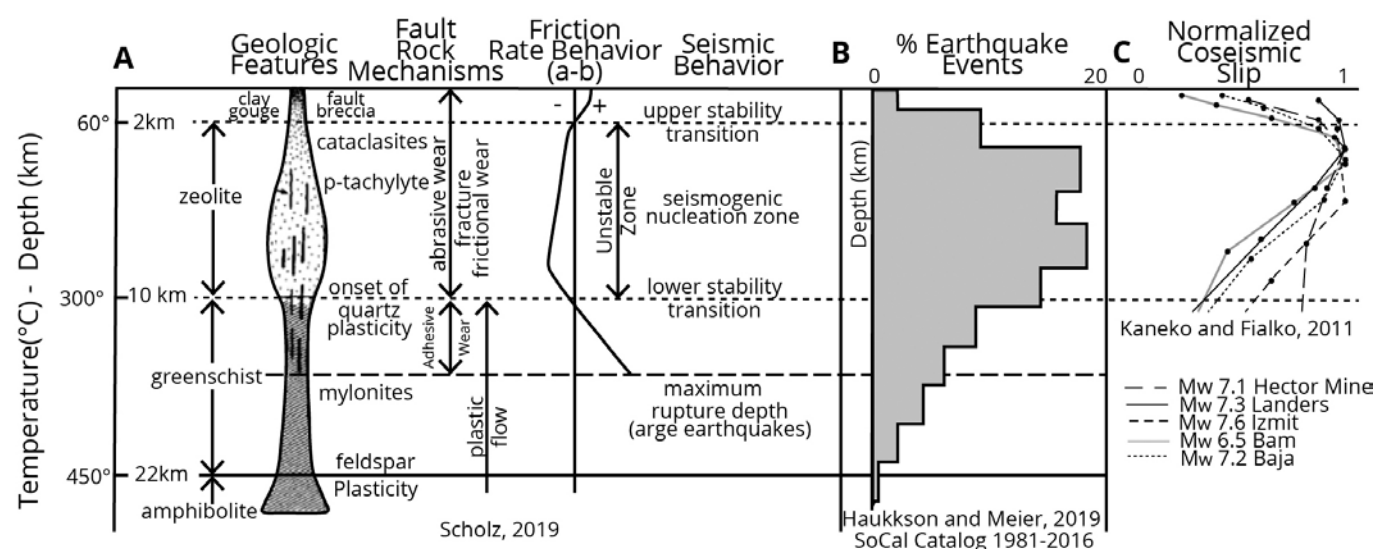


**Figure 1** – Fault and earthquake behavior as a function of depth and temperature, using a southern California geotherm (Williams and DeAngelo, 2011). **(A)** A classic fault vs. depth model, modified from Scholz (2019) and Wibberley et al. (2008). The upper seismogenic transition at ~2-3 km depth is often defined as an unconsolidated and/or clay fault gouge. P-tachylite – pseudotachylite. **(B)** Earthquake depth histogram from Hauksson and Meier (2019) for the Southern California catalog of seismicity (1981-2016). The majority of earthquakes occur at depths of ~2-15 km. **(C)** Normalized coseismic slip distributions of five ~M7 strike-slip earthquakes from model inversions by Kaneko and Fialko (2011). The maximum coseismic slip is interpreted to occur in the seismogenic zone at ~2 to 5 km depth, with coseismic slip sharply decreasing towards the earth's surface, indicating a deficit of coseismic slip may exist in the shallow crust. Approximate temperature gradients from Williams and DeAngelo (2011); metamorphic grades and approximate regions of ductility based on Shinevar et al. (2018).

less affected by surficial weathering and enable us to correlate observations of composition and deformation textures with physical properties derived from borehole geophysical logs. We use samples and data acquired in a geotechnical investigation through the San Gabriel Fault, California (SGF) (Figure 2), which provides access to fault-related rocks that formed at ~2-5 km depth (Bull, 1978; Chester et al., 1993; Blythe et al., 2002) when the San Gabriel Fault was active 5-12 million years ago. We integrate macro- to microscale analyses of the drill core with analyses of outcrop samples and borehole- and core-based rock mechanics data to examine deformation mechanisms and evidence for alteration, fluid-rock interactions, and changes in physical and mineralogical properties of fault-related rocks within the upper fault zone. These data can constrain hypotheses and models of the response of the shallow parts of faults to seismic slip at depth (Roten et al., 2017a; Nevitt et al., 2020) and differentiate among the different hypotheses for the near-surface fault slip deficit observed on faults.

Our work informs and may help revise classic models that depict fault deformation and fault-related rocks as a function of depth and posit that shallow fault-related rocks in the upper ~2-3 km are typically incohesive (Figure 1; Scholz, 1988, 2019; Sibson, 1977; Woodcock and Mort, 2008). However, the composition and structure of active faults may consist of cohesive, altered, and highly sheared rocks (Boulton et al., 2017) and thin fault cores within damage zones comprised of complexly deformed and altered rocks (Chester and Logan, 1986; Chester et al., 1993; Mitchell

and Faulkner, 2009). These aspects of fault zone structure and composition indicate that fault zones may experience complex elastic-frictional and non-frictional behaviors (Figure 1; Marone and Saffer, 2007) that can be constrained by observations of fault-related rocks and fault structure from field analyses or drilled sections of faults.

## 1.1 Geological Setting

The San Gabriel Fault (SGF) in the San Gabriel Mountains, California (Figure 2) accommodated >40 km of right-lateral slip between 12 to 5 million years ago (Powell, 1993; Nourse, 2002) in the early development of the San Andreas fault system. The fault has since been uplifted and exhumed from depths of 2-3 km (Bull, 1978; Chester et al., 1993; Blythe et al., 2002) due to slip on the underlying north-dipping Sierra Madre thrust fault. Evidence for Quaternary slip in the form of aligned canyons, offset Miocene-Pliocene deposits, and the presence of possible degraded fault scarps (Beyer et al., 2009) indicate that as much as 5 km of post-Miocene slip has occurred along parts of the San Gabriel and Vasquez faults (Beyer et al., 2009; Bryant, 2017). Quaternary slip rates of 0.2 to 1 mm/yr estimated for the southern strand of the SGF are ~8-10 times slower than its most active rate in the Mio-Pliocene (Weber, 1982; Yeats et al., 1994; Lee and Schwarcz, 1996). Anderson et al. (1983), Chester et al. (1993) and Evans and Chester (1995) examined surface expressions and samples from the SGF to the southeast of the drill site. Chester et al. (1993) examined rocks exhumed from depths of at least 3.5 km (Blythe et al., 2002), and the sites studied in

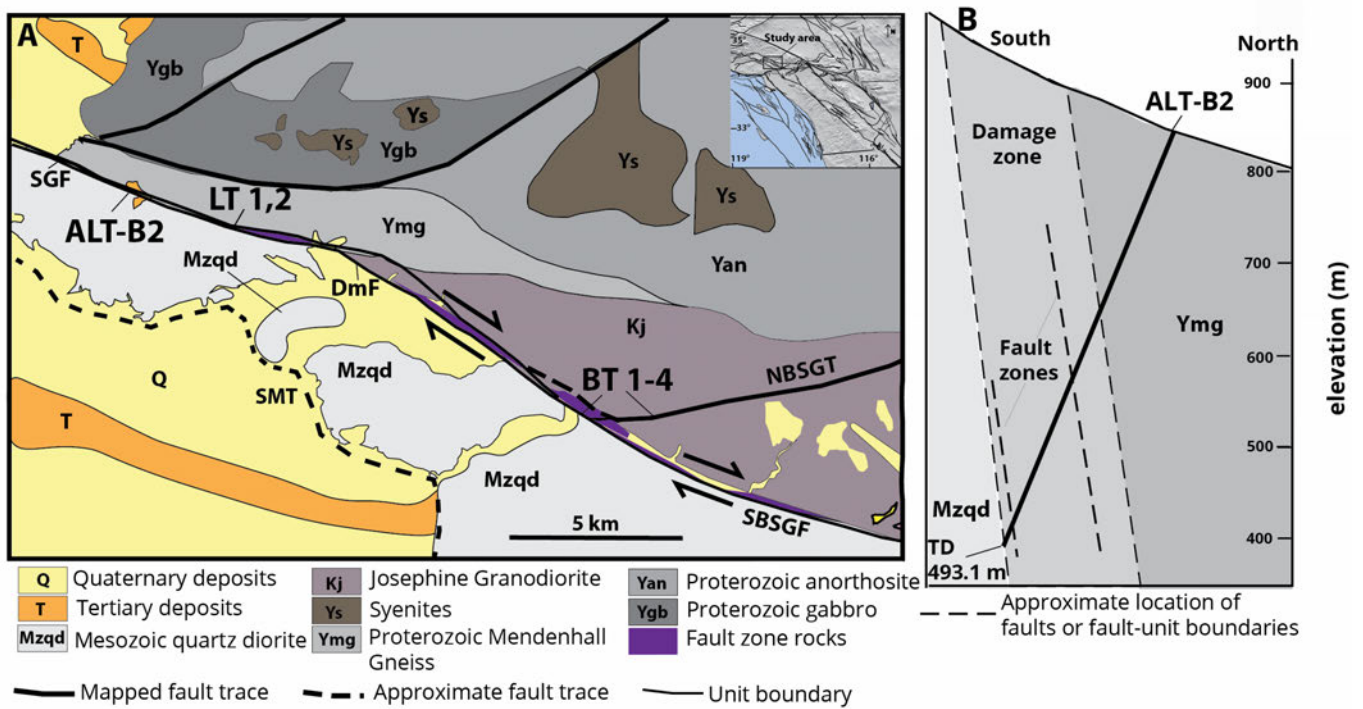


**Figure 2** – Location of the study site. San Gabriel Mountains, southern California. **(A)** Geologic map adapted from *Dibblee and Ehrenspeck* (1991a), *Dibblee and Carter* (2002), and *Yerkes and Campbell* (2005) shows the location of ALT-B2 borehole and Little and Big Tujunga (LT, BT) field sites along the San Gabriel Fault. SGF—San Gabriel fault; SBSGF – south branch San Gabriel Fault, NBSGF- north branch San Gabriel Fault; DmF – DeMille Fault; LT—Little Tujunga; BT—Big Tujunga. SMT – dashed line is the frontal Sierra Madre thrust. The inset map shows the active fault traces from the SCEC Community Fault Model 5.3. The ALT B2 drill hole was located where the San Gabriel fault is mapped as consisting of two closely spaced fault strands. The LT1 and LT2 sites are along the southern strand of the fault, mapped as the DeMille Fault by *Dibblee and Ehrenspeck* (1991a). **(B)** Simplified cross-section adapted from CHSRA drill logs (Guptill, electronic comm., 2017) of the borehole ALT-B2 site. The ALT-B2 borehole plunges 68° south through the steeply north-dipping San Gabriel Fault (SGF) to a total depth of 493.1 m. The geologic descriptions of the rock types are shown in the logs (Figure 3) as is the location of narrow fault zones.

*Anderson et al.* (1983) and field outcrop samples in this work were exhumed ~2 km in the Tujunga fault block (*Blythe et al.*, 2002).

The San Gabriel Mountains are composed of medium- to coarse-grained gneiss, granite, granodiorite, amphibolite, and gabbro of the Proterozoic Mendenhall Gneiss and Cretaceous Mt. Lowe Intrusive rocks (Figure 2; *Anderson et al.*, 1983; *Barth and Ehlig*, 1988; *Campbell et al.*, 2014). Multiple traces of the SGF are mapped along the fault zone and are up to ~100 m apart (*Jennings and Strand*, 1969; *Dibblee and Ehrenspeck*, 1991a; *Dibblee and Carter*, 2002; *Yerkes and Campbell*, 2005; *Campbell et al.*, 2014). In the central San Gabriel Mountains, the SGF splits into the north and south branches, with the south branch joining the Sierra Madre-Cucamonga thrust system to the southeast (Figure 2). Slip along the surface trace of the SGF is confined to a principal slip zone consisting of cm- to m-thick zones of ultracataclasite and foliated cataclasite (*Anderson et al.*, 1983; *Chester et al.*, 1993; *Evans and Chester*, 1995).

### 1.1.1 ALT-B2 Geotechnical Core

The California High-Speed Rail Authority (abbreviated here as CHSRA) collected drill core in 2016 from the ALT-B2 borehole as part of a geotechnical survey across the SGF at depth (Figures 2B, 3). At the ALT-B2 borehole site, the steep north-dipping fault juxtaposes Precambrian Mendenhall Gneiss on the north side against Cretaceous leucocratic granitic rocks interlayered with Cretaceous quartz diorite (Figures 2, 3; *Dibblee and Ehrenspeck*, 1991a). The ALT-B2 borehole was drilled with a plunge of ~68° to 162°, reaching a total drill hole depth (TD) of 493.1 m and a true vertical depth of 457.2 m. The borehole formed a ~32° angle with the ~80° north-dipping SGF zone (Figure 3) and sampled an extensive portion of the fault damage zone and two principal slip zones. The north dip of the fault is determined by connecting the mapped surface trace near the drill site to the shallowest fault core, termed the principal slip zone in this paper, encountered in the fault zone, and from field data for the dip of the fault nearest the drill site.

The ALT-B2 borehole was drilled using an HQ drill rod with an 8.9 cm diameter coring system and spudded at 34.359514°N, 118.398809°W (371364.94E, 3802894.69N, UTM zone 11S) at an



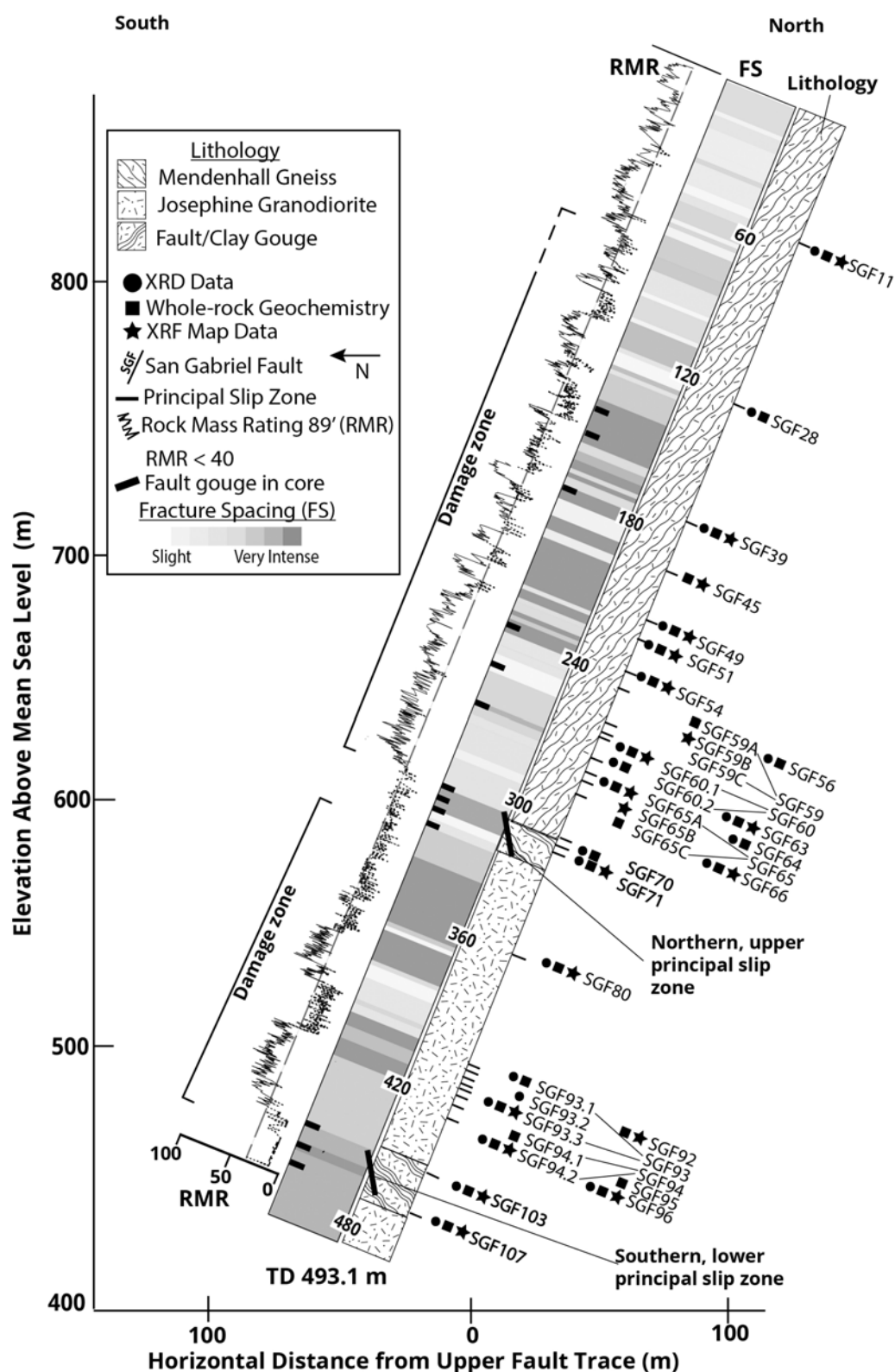


**Figure 3** – Cross-section of the ALT-B2 borehole showing simplified lithology, fracture density measured in core, locations of core samples, geochemical data, and the SGF. The lithologies consist of Mendenhall Gneiss to 313 m depth and Josephine Granodiorite to the bottom of the borehole. There are two principal slip zones, two damage zones, two highly fractured zones, and two zones of lower fracture intensity and sheared rocks recorded in the cored rocks and related rock mass characterization. Fracture density is derived from the core logging, which followed the methods of *Caltrans* (2010) (see Supplemental File 2). Rock mass ratings (RMR) from geotechnical reports are a measure of the core-scale rock strength, based on fracture density, alteration, hardness, and moisture content. Dashed lines indicate the locations of poor to very poor (<40) RMR values, which broadly equate to low values of Young's modulus. The fracture spacing is: slight=30-90 cm spacing; moderate=10-30 cm spacing; intense= 2.5-10 cm spacing; very intense = fracture spacing of <2.5 cm. The Kelly bushing elevation is 864 m MSL. Results do not report ~6 m of surface gravel and soil.

elevation of 864.38 m (2,835.89 ft) above sea level. Poor borehole conditions in the fault zone region of ALT-B2 through the SGF resulted in difficult drilling conditions and “clay-squeezing” in parts of the borehole, and a lack of borehole-based seismic velocity measurements. Geotechnical reports (*HSR, 2019*) provide data on lithology, rock quality designation (RQD), hardness, weathering, fracture density, unadjusted rock mass rating (RMR), and rock mass quality (Q) of nearly 493 m of core. The drill core was sampled at field storage facilities in 2018 and 2019.

### 1.1.2 Little and Big Tujunga Canyon Exposures

Field exposures of the San Gabriel Fault ~4 to 20 km southeast of the ALT-B2 drill site (Figure 2) in Little Tujunga and Big Tujunga canyons provide further insights and samples from the fault zone (see *Anderson et al., 1983*). The main trace of the SGF in Little Tujunga Canyon (sites LT1 and LT2) juxtaposes Mendenhall Gneiss and Josephine Granodiorite, with a small outcrop of Tertiary siltstone and mudstones in the fault zone (*Dibblee and Ehrenspeck, 1991a*) at LT1. The Big Tujunga sites BT1 and BT2 are ~16 km east-southeast of the drill site, where the fault consists of two strands. North of the northern strand, the rocks consist of Cretaceous quartz diorite. The SGF splits into north and south branches and a ~250 m wide zone of faulted and altered gneisses lies within the fault zone and quartz monzonites are south of the zone (Figure 2; *Dibblee and Carter, 2002*). The SGF at these sites exhibits thin ultracataclasite zones, gouge zones, and zones of brecciation and damage (*Anderson et al., 1983; d'Alessio, 2004*).

## 2 Methods

We document the physical and mineralogic properties of fault-related rocks and examine the evidence for deformation, fluid-rock interaction, and changes in mineralogy within rocks that formed at depths of 2-3 km in the upper SGF. Integrated macroscopic drill core and outcrop analyses, optical microscopy, and X-ray diffraction mineralogic analyses are used in conjunction with borehole-based measurements of fracture densities and rock mass rating data (*HSR, 2019*) to determine the fault zone structure, deformation mechanisms, and alteration patterns. Here we focus on the macroscopic and microstructural nature of the deformed rocks from drill core samples and supplement them with data from outcrop samples from the Little and Big Tujunga canyons. The ALT-B2 drill core dataset includes borehole data provided by the *HSR (2019)*, 28 core samples, 28 thin sections, and 34 X-ray diffraction (XRD) measurements (Supplemental Files). The field sample dataset consists of 26 field samples and 34 thin sections.

Mesoscopic analyses of the drill core document the lithologies, shear fabrics, nature of the alteration,

intensity of deformation, and the distribution of veins, slip surfaces, and other indicators of fluid-rock interactions. The ALT-B2 borehole sampled a large portion of the fault damage zone, with an average drill core recovery rate of 95%. Samples we examined in detail consist of 5.12 m of drill core from 28 sites along the core (Figure 3; Table 1). Drill core samples were selected to encompass the entirety of the drill core and to target protolith and fault-related rocks within the principal slip zones and damage zones. The samples were typically well-indurated. We compiled the fracture density data and the geotechnical rock mass rating from the geotechnical data to determine the physical properties of the cored rocks. We used geotechnical rock-mass characterization data (*HSR, 2019*) to constrain the mechanical properties of the rocks (Figure 3). Rock-mass classification schemes are used in geotechnical studies to report Rock-Mass Rating values, denoted as RMR (*Bieniawski, 1993; Aydan et al., 2014*). These are based on six rock quality descriptors (Supplemental File 8) to provide qualitative estimates of frictional and cohesive rock strengths from 0 to 100, where 0 is a rock mass with no cohesion or frictional strength, and 100 is for an intact rock mass.

The up-dip and along-strike parts of the SGF exposed in Little and Big Tujunga Canyons (Figure 2) were sampled by J. S. Caine in 1993 and characterized by D. Forand and J. Jacobs in 2002. We made qualitative descriptions of rocks at 6 sites along the fault zone and used data, images, and hand samples (Supplemental File 3), to establish their provenance relative to the faults and provide small-scale structural data. These field sites are discussed in *Anderson et al. (1983)* and Supplemental File 3. We used 38 thin sections from these field sites.

We employed optical microscopy to examine grain-scale deformation and the textural composition of the fault-related rocks, the relationships of grains to surrounding material, and the evidence for the interaction of minerals, shearing, and fluid-rock interactions (*Schulz and Evans, 1998, 2000; Bradbury et al., 2015*). Twenty-eight standard (27 × 46 mm × 30 μm) and 11 large (51 × 77 mm × 30 μm) probe-polished thin sections from the ALT-B2 core, and 26 standard and 8 large thin sections from the field samples were examined. Entire thin-section scans were made using an Epson Perfection Pro scanner in plane-polarized and cross-polarized light. We use our microscopic observations to search for evidence for grain-scale brittle, crystal-plastic, diffusive mass transfer, and alteration-related deformation (c.f., *Rutter, 1986; Blenkinsop et al., 2020; Wang, 2021*).

Systematic X-ray diffraction (XRD) analyses were done to determine whole-rock mineralogy and to constrain rock compositions, possible depth ranges, and fluid-rock interactions in the fault-related rocks.

**Table 1** – Summary of the location of the core samples for this research. Drill runs are recorded as the box number and the nomenclature of the sample names (see Figur 3) is tied to these numbers. Depths of the samples, originally measured in feet and converted to meters, are shown, and these are used in conjunction with the entire core logs (HSR, 2019) to constrain the subsurface geometry of the fault zones.

Core Box	Core Sample Name	Measured Depth ALT-B2 From (m)	To (m)	Distance from PSS along ALT-B2 (m)	Horizontal Distance from PSS (m)
11	SGF11	55.87	56.05	257.1	138.4
28	SGF28	127.71	127.88	185.3	99.7
39	SGF39	177.45	177.70	135.5	72.9
45	SGF45	202.94	203.00	110.1	59.2
49	SGF49	223.17	223.27	89.8	48.3
51	SGF51	229.54	229.70	83.5	44.9
54	SGF54	244.36	244.60	68.6	36.9
56	SGF56	251.00	251.19	62.0	33.4
59	SGF59A	266.70	266.84	46.3	24.9
59	SGF59B	266.84	266.95	46.2	24.8
59	SGF59C	266.95	267.01	46.0	24.8
60	SGF60.1	267.31	267.45	45.7	24.6
60	SGF60.2	269.81	270.05	43.2	23.2
63	SGF63	281.57	281.80	31.4	16.9
64	SGF64	287.91	288.22	25.1	13.5
65	SGF65A	291.24	291.51	21.8	11.7
65	SGF65B	291.51	291.74	21.5	11.6
65	SGF65C	291.65	291.80	21.4	11.5
66	SGF66	295.85	295.95	17.1	9.2
70	SGF70	314.61	314.78	1.6	0.9
71	SGF71	315.86	316.00	2.9	1.5
80	SGF80	360.73	360.85	47.7	25.7
92	SGF92	408.43	408.65	95.4	51.4
93	SGF93.1	413.26	413.48	100.3	54.0
93	SGF93.2	413.52	413.64	100.5	54.1
93	SGF93.3	416.28	416.45	103.3	55.6
94	SGF94.1	417.32	417.52	104.3	56.1
94	SGF94.2	418.87	418.96	105.9	57.0
95	SGF95	420.76	420.85	107.8	58.0
96	SGF96	426.28	426.43	113.3	61.0
103	SGF103	456.44	456.53	143.4	77.2
107	SGF107	472.27	472.41	159.3	85.7

Fluid-rock interactions alter the mineralogy of rocks (Warr and Cox, 2001; Callahan *et al.*, 2020), and mineralogic variations (Ishikawa *et al.*, 2008, 2014) can indicate the nature of the fluids that may have interacted with the rocks. Field, protolith, damage zone, and principal slip zone samples were sub-sampled to document minute changes in mineralogy, variations in distance from the principal slip surface, slip surface compositions, and relative abundances. Whole-rock geochemical data and X-ray fluorescent maps of thin sections of these samples are discussed in Evans *et al.* (2023). X-Ray Diffraction data were collected and analyzed using the PANalytical X'Pert PRO X-Ray diffractometer at USU Geosciences X-ray Diffraction Lab. Approximately 10-20 g of crushed rock samples were crushed to a homogenous powder in a tungsten carbide bowl using a ROCKLABS Ring Mill Pulverizer in USU's Rockprep Lab. One g of whole-rock powder

sample material was analyzed in an aluminum sample plate from 2-75° at X-Ray conditions of 45 kV and 40 mA at one second per 0.02° step increments. Mineral phase identification was interpreted using the PANalytic X'Pert HighScore program version 4.5 and the ICDD PDF- 4+ Inorganic database of reference patterns. The range of potential mineral phases was further refined based on the XRF data results and petrographic analysis. Mineral candidates with high scale and score factors were prioritized, then phases were user-matched to the position and intensity of the reference patterns match to sample peaks. We did not perform clay-specific XRD analyses, and in samples where clay is abundant, the clay mineral phases were identified based on a match to reference patterns in the database. Sample locations, descriptions, and X-ray diffraction data summaries are provided in Supplemental File 1.

## 3 Results

### 3.1 Macroscopic Descriptions

The host rock of the ALT-B2 core consists of Mendenhall Gneiss on the north side of the fault zone to 313 m measured depth (mmd) along the borehole, with minor igneous intrusive rocks, and Josephine Granodiorite from ~313 mmd to the bottom of the borehole (Figures 3, 4) on the south side of the fault. Two principal slip zones are recorded in the ALT-B2 core, corresponding with indurated fault/clay gouge recorded at 313-325 mmd and 456.5-476.5 mmd along the borehole (Figures 3, 4). The upper principal slip zone at 313-325 mmd coincides with the lithologic change from the gneissic rocks to the north and the granodiorite to the south of the SGF. We interpret this as the main fault zone, as do the geologists in the draft geotechnical report (HSR, 2019). Correction for the obliquity of the drill hole suggests that this principal slip zone has a true thickness of about 6.5 m. The lower principal slip zone is 11 m thick. It is embedded within the Josephine Granodiorite and forms a sharp margin with the damage zone of the SGF. The drill hole did not continue beyond this zone, however, so that relationship is not certain (Figure 3). The lowermost ~20 m of the borehole encountered a third zone of low Rock-Mass Rating (RMR) values.

Fracture data presented in the geotechnical study (Supplemental File 2) documents the nature and distribution of fractures along the borehole. Fracture density varies from slight to very intense (Figure 3; Figure S2.3A), and fracture dip increases with depth (Figure S2.3B). Zones of high fracture intensity are found at 140-160, 200-230, and 340-370 mmd. The fracture spacing is relatively less intense directly north of the principal slip zones, with a ~40 m wide zone of slight-moderate intensity north of the upper principal slip zone and a 15 m wide zone of moderate intensity north of the lower principal slip zone (Figure 3; Figure S2.3A). The rocks in these lower-intensity fracture zones have higher RMR1989 values and exhibit evidence of shearing and folding, with few preserved fractures and veins. We observe lozenges of relatively unaltered to slightly altered protolith around 61 m and 25-30 m north of the main SGF trace (at 251 mmd and 280-288 mmd in the borehole).

The rocks in the ALT-B2 borehole exhibit fault damage zones that extend ~60 m to the north and ~30 m to the south of the upper principal slip zone. The damage zones are defined by intense to very intense fracture spacing, the presence of sheared rock (Figure 4; Supplemental File 4), and altered and damaged rock assemblages. Zones of poor to very poor RMR1989 values (<40) are recorded at 104-120 mmd, 145-160 mmd north of the upper principal slip zone in ALT-B2, a zone up to 60 m south of the upper principal slip zone (310-390 mmd), and a zone at 405 to 416 mmd. Numerous zones of low RMR1989 are found through the borehole (Figure 3;

Supplemental File 8), including at the principal slip zones of 313-325 mmd and 456.5-476.5 mmd. These low RMR1989 values indicate that these rocks consist of a combination of low uniaxial compressive strength, high fracture spacing, fracture orientations, high water saturation, and poorly indurated rock (Bieniawski (1989).

Up-dip and along strike exposures of the San Gabriel Fault south-southeast of the drill site at the Little Tujunga Canyon sites (Figure 5, Supplemental File 3) show that the fault juxtaposes slivers of Eocene sedimentary rocks (Dibblee and Ehrenspeck, 1991a) and the Josephine Granodiorite on the north across an ~4 m thick zone with a 1-4 cm thick cataclasite zone that dips steeply southwest (Figure 6A-C). Closely spaced fractures and a cleavage-like planar fabric are present within the fault zone, which is variably mapped here as comprising one or several strands along the strike (Dibblee and Ehrenspeck (1991a). At site LT2 (Figure 5), the steep northeast-dipping fault (Figure 6D) exposes Mendenhall Gneiss to the northeast on Josephine Granodiorite to the southwest (Anderson et al., 1983). At both sites, the fault core is composed of a 1-4 cm thick dark brown to black ultracataclasite zone (Figure 5C; Anderson et al., 1983; J. S. Caine, written comm., 2019). The Josephine Granodiorite is highly fractured and altered up to 15 m away from the fault core. The small faults and fractures are mostly at high angles to the main fault surface (Figure 6A-B), and quartz and epidote veins are subparallel to the main fault strand (Figure 6C). At site LT2, the damage is expressed primarily as fractures at a range of orientations. Veins are subparallel to the fault (Figure 6D) and zones of alteration in the gneiss. At ~5-6 km east-southeast of the LT1 and 2 sites, roadcuts reveal a series of steeply southwest dipping faults that are several meters to ~17 m thick (Supplemental File 3).

Fracture density as determined from the acoustic image logging tool run in the borehole (Figure 6E-F) shows that fractures in the rocks are concentrated in two groups. Most fractures dip moderately northeast and strike northwest, and a subordinate group dips steeply southwest and strikes southeast. Fracture dips show a slight trend of increased dips with depth (Supplemental File S 2.4), but as in the core data, the changes are slight. Big Tujunga sites BT 1, 2, and 4 (Sites 10, 11, and 14 of Anderson et al., 1983) reveal the North Branch of the San Gabriel Fault is expressed as a series of fault strands in weathered outcrops ~1 km east of the branch point with the South Branch of the fault (Supplemental File 3; Ehlig, 1973; Dibblee and Carter, 2002). The fault zone here juxtaposes Cretaceous quartz diorite and granodiorite (the Wilson Diorite) on the southwest side of the fault, and Cretaceous quartz monzonite and granodiorite, and the Josephine Granodiorite to the north (Dibblee and Carter, 2002). Here the fault zone is an up to 4-7 cm thick cataclasite with a 70 m thick foliated shear zone that dips steeply southwest



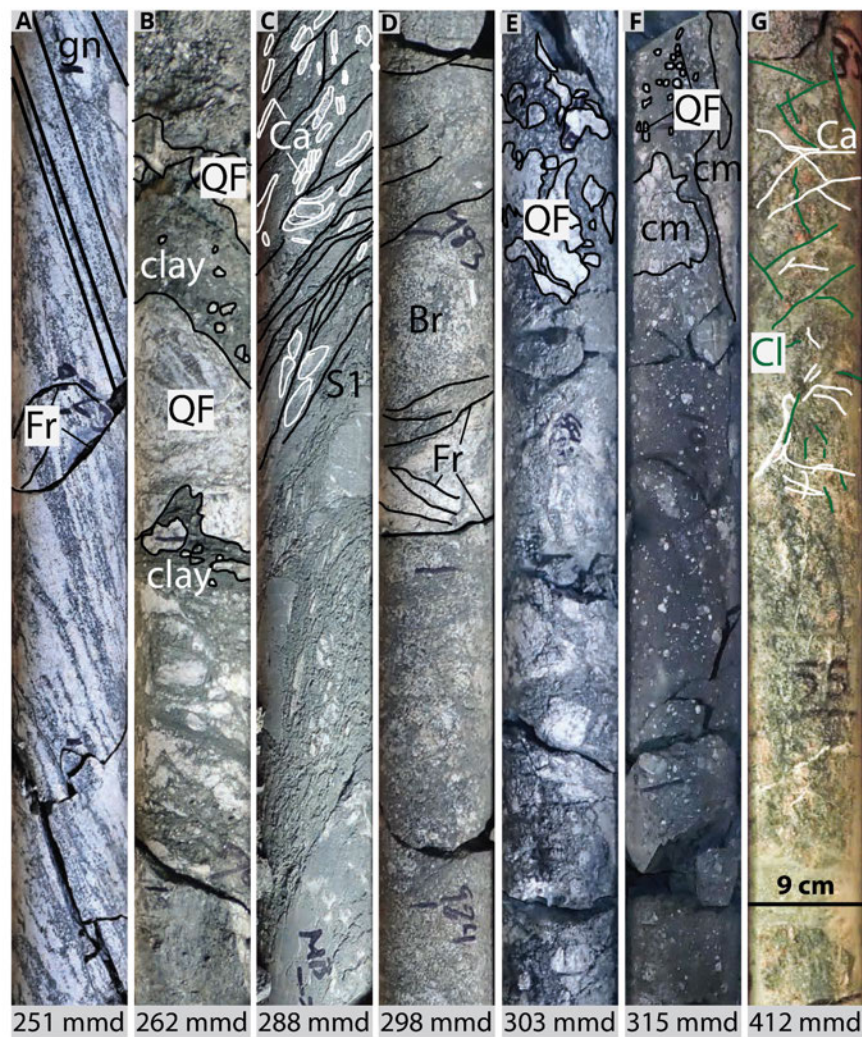


**Figure 4** – Annotated photographs of cores that document the rock types and deformation textures sampled by borehole ALT-B2. Down is to the bottom of the page, and sample depth is labeled at the bottom of the core. **(A)** Relatively undamaged gneissic protolith with gneissic banding (gn) cut by fractures (Fr). **(B)** Clay-rich gouge and breccia damage zone rock with quartzofeldspathic (QF) clasts, from gneissic protolith. **(C)** Foliated cataclasite with penetrative fabric (S1) and elongated carbonate (Ca) clasts, from gneissic protolith. **(D)** Highly indurated breccia (Br) zones composed of angular fragments and cut by brittle fracture (Fr), from gneissic protolith. **(E)** Brecciated damage zone rock with random-fabric breccia with quartzofeldspathic (QF) clasts. **(F)** Well-indurated cataclasite with comminuted quartzofeldspathic clasts (qf) and zones of cementation (cm), from the upper principal slip zone. **(G)** Highly altered damage zone in the lower damage zone, with cross-cutting chlorite (Cl) and calcite (Ca) veins, small faults, and an overall chlorite-zeolite alteration texture that overprints the Josephine granodiorite protolith.

(Supplemental File 3). One sheared sequence is ~6m thick and consists of an anastomosing network of brecciated fault clasts in a zone of polished and striated slip surfaces. In places, 2-5 m thick zones are composed of chloritically altered granodiorite and altered quartz monzonite. Thin, 5-10 cm-thick black and dark brown fault zones are composed of foliated gouge and ultracataclasites and show sharp boundaries with damaged rocks. The likely main fault zone dips steeply southwest, and the few related slip surfaces dip steeply around the main fault surfaces (Figure 5E). At the eastern end of the outcrop at BT2, a fault strand is as much as 40 m thick with a fault-related foliation that dips steeply north.

### 3.2 Mesoscopic Observations

We divide the fault zone into protolith, damage zones, and principal slip zones (*Caine et al., 1996; Wibberley and Shimamoto, 2003*) based on mesoscopic observations of the core (Supplemental File 4) and outcrops, geotechnical reports, and distance from the principal slip surface (Figures 4, 7). Drill core samples are highly indurated and the core recovery rate was 95% (Supplemental File 3). The rocks in the upper part of ALT-B2 consist of slightly to moderately deformed protolith of the felsic Mendenhall Gneiss (Figure 4A). These rocks exhibit cm-scale gneissic banding defined by feldspar-rich (primary albite to oligoclase) and hornblende ± biotite-rich layers. Gneissic protolith samples are differentiated from damage zone samples by the



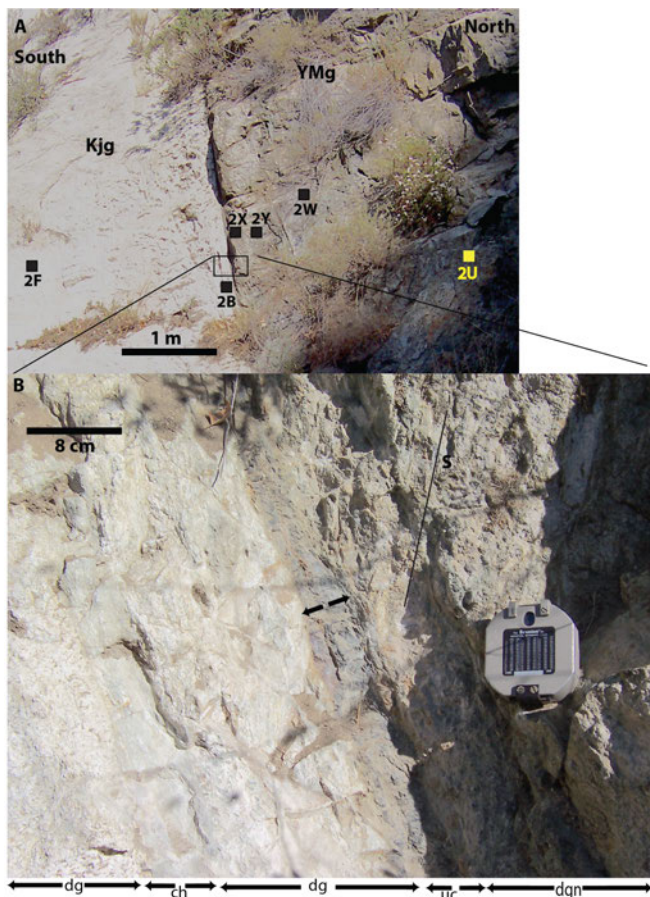


**Figure 5** – Photographs of rock exposures at field site LT2 of the San Gabriel Fault. This is the Earthquake fault site 8 of *Anderson et al.* (1983). **(A)** View to the northwest of the steep northeast dipping fault with Mendenhall Gneiss (YMg) juxtaposed against the Josephine Granodiorite (Kjg). Boxes indicate the locations of samples used for thin sections (Supplemental File 7). **(B)** Close-up view of the fault, with a 5 cm thick ultracataclasite zone (UC), with a fault-related foliation fabric (S) in the gneiss, and the fractured and brecciated damage zone (dg) and chloritic sheared rock (ch) in the Josephine granodiorite. The damage zone in the gneiss (dgn) is ~30 cm thick and is the outer boundary of the damaged rocks.

presence of well-defined gneissic banding of altering light and dark bands and minerals that are easily recognizable (Figures 4A; 7A, B). The Mendenhall Gneiss experienced high-grade Precambrian granulite-grade and Mesozoic greenschist-grade metamorphism (*Anderson et al.*, 1983; *Barth et al.*, 1995a). The borehole does not sample undamaged igneous rock from the Josephine Granodiorite, but in the outcrop, relatively undamaged rock of the Josephine Granodiorite and the Mendenhall Gneiss are present.

The damaged zones exhibit fault-damaged rocks (Figure 4B-G) with a variety of deformation textures, including foliated cataclasite, brecciated zones, fractures, small faults, veins, discrete slip surfaces, iron-oxide coatings, and sheared zones (Figure 7C-H). Many samples show multiple types of deformation and cross-cutting relations. Sheared samples in the damage zones directly north of the upper

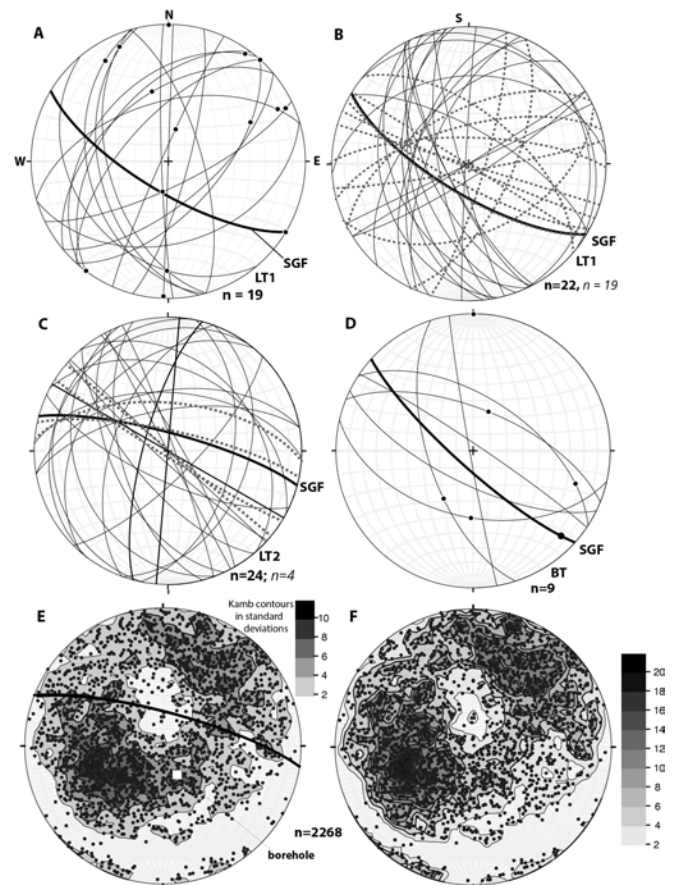


**Figure 6** – Lower hemisphere equal area stereograms of orientation data of structures related to the San Gabriel Fault, as viewed in outcrops in outcrops at the Little (LT) and Big Tujunga (BT) canyon sites, and from borehole-based image data. **(A)** Fault orientation data from the LT exposures – the great circles represent the orientations of the faults and the dots show the orientation of the slip vectors. The bold great circle represents the orientation of our interpretation of the main San Gabriel Fault at this site (see Figure 5). **(B)** Orientations of fractures and veins in the damaged zone from the LT 1 site. Veins are blue dashed great circles. **(C)** Orientations of the main San Gabriel Fault, fractures, and veins (in blue dashed great circles) at the LT2 site. **(D)** Orientation of the main San Gabriel Fault and small faults exposed at the BT 2 and 4 sites. **(E)** Poles to fractures recorded from acoustic televiewer data in the borehole. Fracture data are in Supplemental File 3. The orientation of the borehole is indicated by the white square. **(F)** Poles to fractures from the acoustic televiewer data adjusted using a Terzaghi correction for orientation bias along a linear traverse—plots, and methods used by *Allmendinger et al.* (2011) and *Cardozo and Allmendinger* (2013)

and lower principal slip zones (Figure 3) exhibit folding of foliated cataclasite and penetrative shear fabrics, with generally fewer and smaller preserved veins (Figure 7D, F, H). Some veins in the sheared rock show cross-cutting relationships with existing cataclastic foliations (Figure 7F). Veins visible in the Josephine Granodiorite damage zone south of the upper principal slip zone are larger and more abundant than those preserved in damaged rock in the Mendenhall Gneiss north of the upper principal slip zone, with veins up to 1.5 cm wide and >20 cm



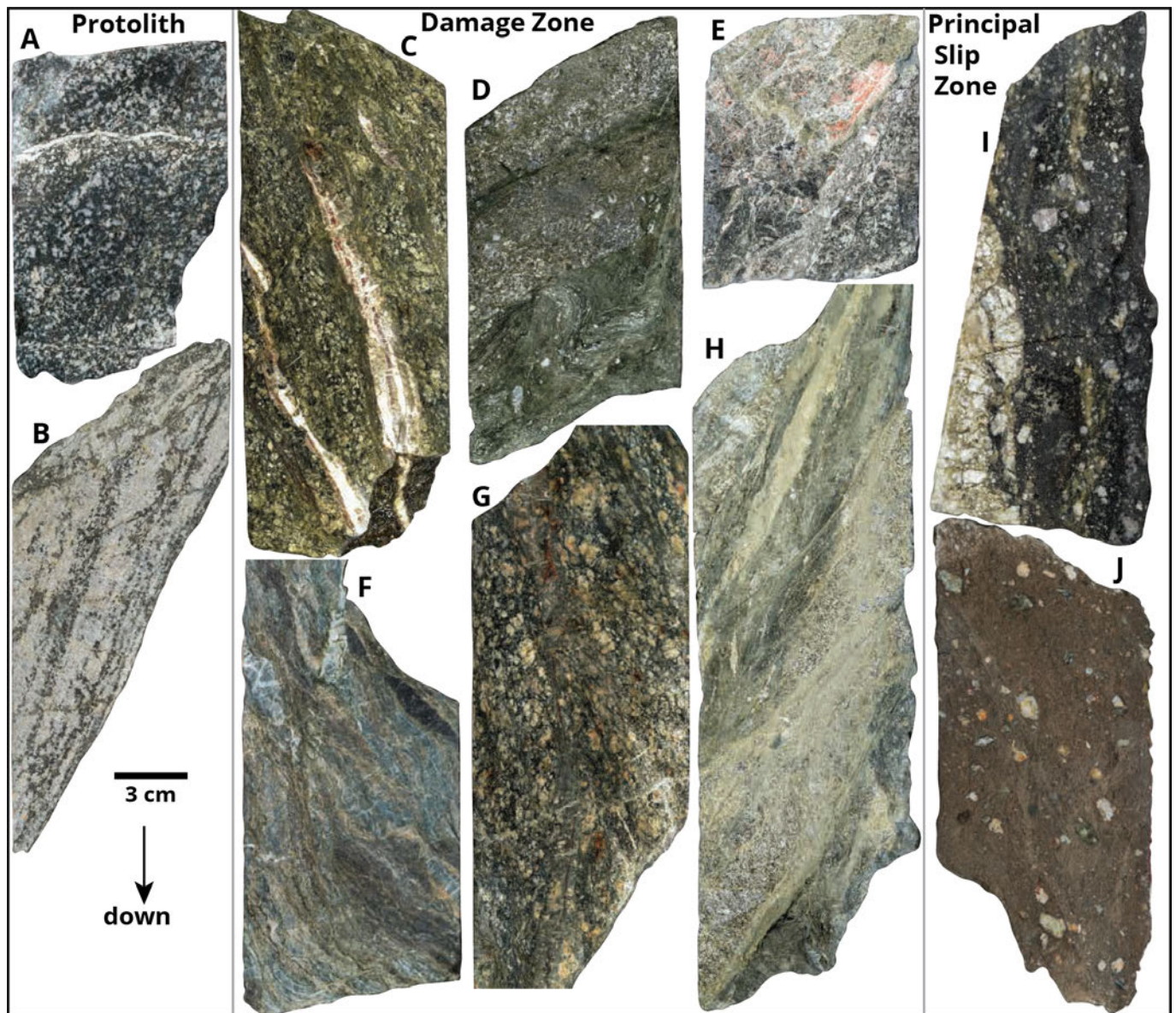


**Figure 7** – Photographs of cut faces of hand samples of cored pieces of the protolith, damage zone, and principal slip zone rock. **(A)** Protolith samples show slightly deformed amphibolite with sparse to no foliation, and **(B)** foliated gneiss. **(C-E)** Damage zone zones consist of altered and damaged rocks that show foliated cataclasite **(D)**, breccia **(E)**, veins **(C, D, E)**, and iron oxides **(C)**. **(F-G)** Strongly foliated, highly sheared damage zone rocks with discrete slip surfaces **(F)**. **(G)** Brecciated and chloritically altered rocks. **(I-J)** Principal slip zone exhibits gouge, clay, cataclasite, and ultracataclasite. Sample names and measured depths are: **(A)** SGF11, 55.9-56.1 m exhibits either no to poorly defined foliation in a mafic-rich zone. **(B)** SGF56, 251-251.2 m, has a well-defined gneissic fabric. **(C)** Sample SGF93.3, 416.3-416.45 m in the lower damage zone with carbonate+zeolite veins that cut a chloritically altered gneiss. **(D)** SGF60.1, 267.3-267.45 m, with a mafic-rich sheared rock. **(E)** SGF94.2, 418.9-419 m - chlorite-epidote-zeolite-carbonate altered diorite. **(F)** SGF96, 426.3-426.45 m, penetratively sheared chlorite zone. **(G)** SGF92, 408.4-408.6 m, brecciated gneissic section. **(H)** SGF54, 244.4-244.6 m, intensely sheared zone. **(I)** SGF71, 315.9-316 m, cataclasite with light fragments of earlier-stage breccia in the dark aphanitic cataclasite. **(J)** SGF103, 456.4-456.5 m, lower cataclasite to ultracataclasite with rounded quartz-feldspathic fragments in the matrix.

long (Figure 7C). Rocks in the deformed Josephine Granodiorite experienced significant deformation and alteration (Figure 4G), indicated by the light-to medium-green chloritic rocks and pink, white, and red fine-grained materials that suggest the presence of carbonates, iron-oxides, and hydrothermally altered feldspars. The drill core in the granodiorite damage zone tends to be slightly less indurated than the drill core from the gneissic damage zone (Supplemental File 3).

The principal slip zones consist of cataclasite,

ultracataclasite, and moderately indurated clay gouge proximal to and within the fault (Figure 4F). Samples from the upper principal slip zone exhibit cataclasites, shear surfaces, and fractures (Figure 7I). The zone we interpret as the main fault core is ~6.5 m thick measured perpendicular to the fault zone, and is comprised of black aphanitic gouge material with mm- to cm-scale angular to rounded fragments of brecciated and altered fragments of gneiss. The samples from the lower principal slip zone exhibit very fine-grained fault-related rocks such as

ultracataclasite and relatively well-indurated clay fault gouge (Figure 7J). The rocks from the field sites (Figure 8; Supplemental File 5) range from protolith Josephine granodiorite (Figure 8A-B), foliated and fractured gneiss (Figure 8C), indurated leucocratic breccias and cemented cataclasites (Figure 8D-E), indurated chloritic cataclasite (Figure 8F-G), and aphanitic ultracataclasite (Figure 8H).

### 3.3 Microstructures and Alteration Textures

Thin sections span the length of the ALT-B2 borehole and sample each rock type identified in the drill core (Figures 9- 12; Supplemental File 6). The protolith samples consist of slightly to moderately fractured gneiss and a suite of intrusive igneous rocks with quartz, relatively unaltered feldspar, biotite, and hornblende grains (Figure 9). The rocks from the damage zone and adjacent to the principal slip surfaces exhibit a range of deformation fabrics, alteration textures, and evidence for mineralization.

Gneissic foliation of the Mendenhall Gneiss in the core is defined by 0.1 to 3 cm-wide bands of leucocratic and mafic mineral zones (Figure 9A, C). The rocks consist of hornblende- and plagioclase-rich zones and, in places, mafic-rich zones with rounded leucocratic enclaves (Figure 9B). In parts of the gneiss, the foliated fabric is largely absent (Figure 9A). The Mendenhall Gneiss exhibits retrogression in which original pyroxene and garnets are replaced by hornblende + biotite + calcite + epidote + quartz (Barth *et al.*, 1995a). The protolith gneiss is cut by thin intra- and intergranular fractures, discrete slip surfaces, and quartz or calcite veins (Figure 9A). Undeformed Josephine intrusive suite samples from field sites (Figure 9E-H) consist of diorite, tonalite, and granodiorite (Barth and Ehlig, 1988) intruded at a depth of ~20 km. The Big Tujunga samples reveal equant-to-subsequent quartz grains in altered feldspars (Figure 9E, F, H), elongated zones of hornblende + biotite, and evidence of retrogression of the feldspars and hornblende-biotite regions (Figure 9F). Slip surfaces that cut the granodiorite appear to link transgranular fractures that link the feldspar and mafic mineral zones (Figure 9G, H).

Damage zone samples exhibit a range of fracture patterns, micro breccias, gouges, foliated cataclasites, breccia, shear zones, fractures, veins, zones of chloritization, and Fe-oxide-rich slip surfaces and zones (Figures 10- 12). Damage zone rocks 10-40 m from the upper principal slip surface have inter- and intragranular fracture patterns that form areas of incipient alteration and cataclasis (Figure 10A-C). In places, irregular zones of chloritic alteration (after biotite and hornblende) developed (Figure 10D) and were folded (Figure 10E). Breccia samples exhibit Fe-oxide/chlorite- and micro breccia-rich matrices, and the cementation of quartzofeldspathic grains. These quartzofeldspathic clasts exhibit micro- and intragranular fractures and

mosaic fracture textures (Figure 10D). Many of the primary hornblende grains grades are degraded to chlorite in the damage zone.

The intensity of these fabrics varies throughout the damage zones but tends to be more strongly expressed near the principal slip surfaces. Multiple generations of cataclasis are indicated by the presence of cemented, rounded clasts of cataclasite incorporated in chloritic gouge zones (Figure 11A). Thin zones of cataclasite appear to evolve from highly fractured protolith (Figure 11B). Highly deformed cataclasites exhibit foliations (Figure 11C), defined in many places by the development of clay-rich zones (Figure 11D). Cataclasites exhibit a chlorite-rich, folded, and refolded folia, some disarticulated, juxtaposed against breccia (Figure 10E).

Evidence for alteration and mineralization includes the presence of calcite veins, the development of clay and chlorite, zeolite-rich zones, and cementation textures (Figures 12, 13). Calcite veins are common (Figure 12A). Elongate vein fragments composed of carbonate and zeolite layers in porphyroclasts lie within fault gouges and breccia (Figures 11D, 12B). The laminated horizons of clay-rich sheared surfaces (Figure 11B) are elongated parallel to the foliation defined by iron oxide and clay-rich layers. Zeolite-calcite zones are folded near principal slip surfaces (Figure 12C) and veins are cut by narrow slip surfaces and cataclasite (Figure 12D).

Samples of the principal slip zones (Figure 13) consist of foliated cataclasites, ultracataclasites, micro breccias comprised of carbonate-zeolite clasts, and very thin surfaces. The principal slip zones exhibit banding of concentrated iron oxide, calcite, and/or clay-rich material and brecciated and deformed host rock (Figure 13A, B). Millimeter-thin slip surfaces and ultracataclasite zones lie next to cemented cataclasite (Figure 13A). Ultracataclasites contain rounded to elongated fragments of host cataclasite (Figure 13B), and visible at the mesoscopic level, with veins up to 1.5 cm wide and >20 cm long, while veins in the damaged rock north of the main principal slip zone are mostly visible only at the microscale.

The upper principal slip zones consist of cataclasite, ultracataclasite, and well-indurated clay gouge cemented microbreccia with subrounded to subangular to angular fragments of carbonate veins from the damage zone (Figure 13C, D). The fault gouge exhibits highly fractured and possibly cemented, quartzofeldspathic damage zone clasts showing the effects of early cataclasis, healing, and further shearing and alteration. Cross-cutting relationships indicate that breccias formed early, followed by fine-grained cataclasites that were cut by carbonate veins. Both the breccias and cataclasites are isoclinally folded and are cut by narrow slip surfaces (Figure 13D). This folding was likely due to simple shearing in the fault zones.



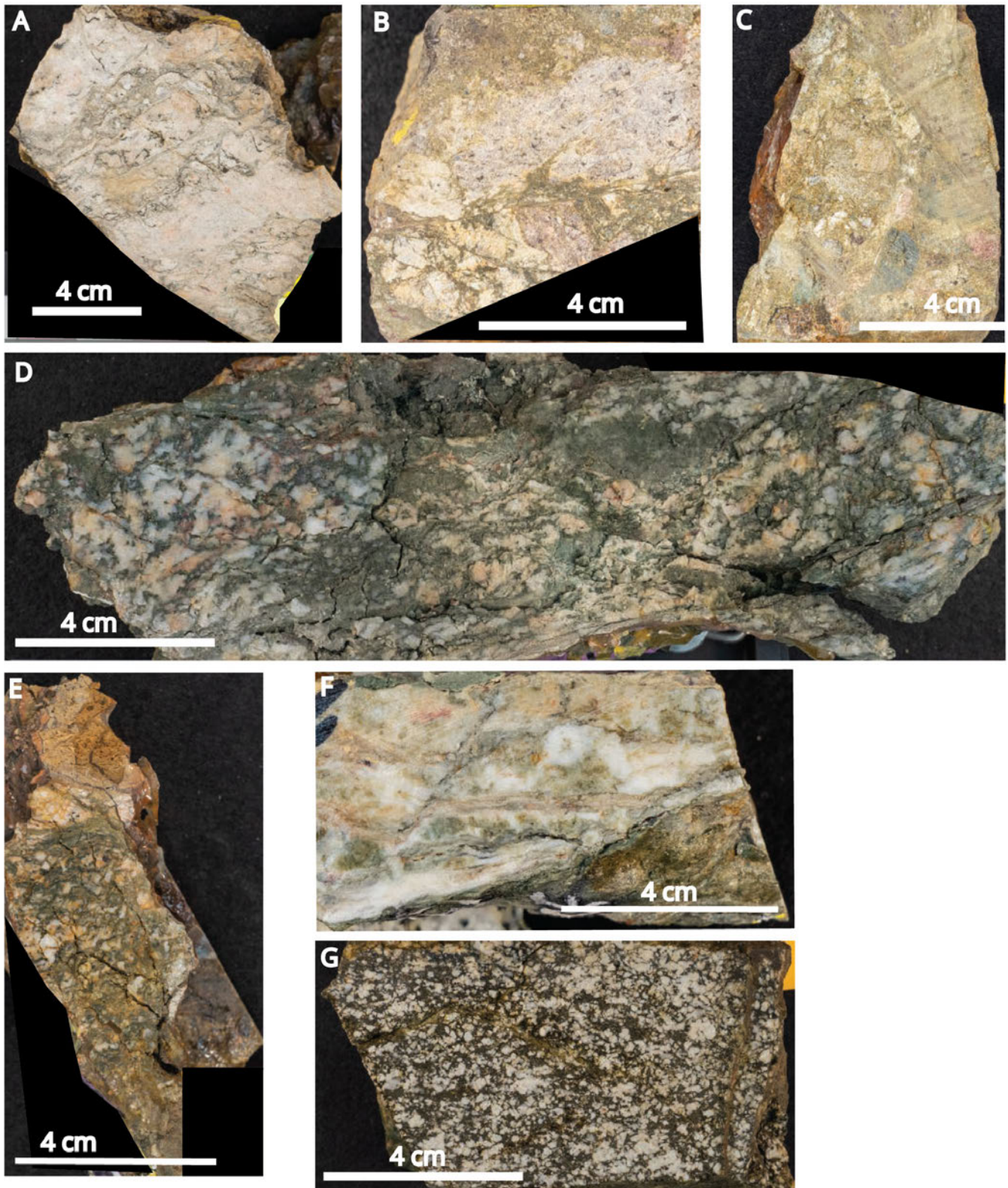


**Figure 8** – Photographs of slabbed faces of hand samples of fault-related rocks from outcrop exposures. **(A)** Sample LT2F of chloritic sheared and cataclastically deformed Josephine Granodiorite from ~3m from the fault zone (see Figure 5). Incipient foliation is defined by cm-scale zones of chloritic sheared rock and lighter brittle breccia. See Figure 10D for the thin section from this sample. **(B)** Sample LT1X from ~2 m north of the San Gabriel fault at the LT1 site, with leucocratic breccia and cataclasite. Fine-grained cataclasite exhibits an injection fracture (**I**) at a high angle to the fault surface. **(C)** Random fabric fault breccia sample LT1Z in the damage zone of the fault in Mendenhall Gneiss. Angular fragments of dark gneiss and light fault breccia fragments from 2 m north of the fault at the LT1 site. **(D)** Sheared, brittlely deformed, and highly altered gneiss sample BT4C from ~1 m north of the fault zone. Sheared surfaces form a network of through-going surfaces that cut deformed grains. **(E)** Breccia and cataclasite sample LT4A. **(F)** Intensively veined and sheared zone from ~10 cm a principal slip surface at the LT4 site. Most of the sheared rock consists of mm- cm-thick calcite and zeolite zones, in some cases folded. **(G)** Incipient brittle deformation and chloritic cataclasite, and in sample LT4W of the Mendenhall Gneiss.



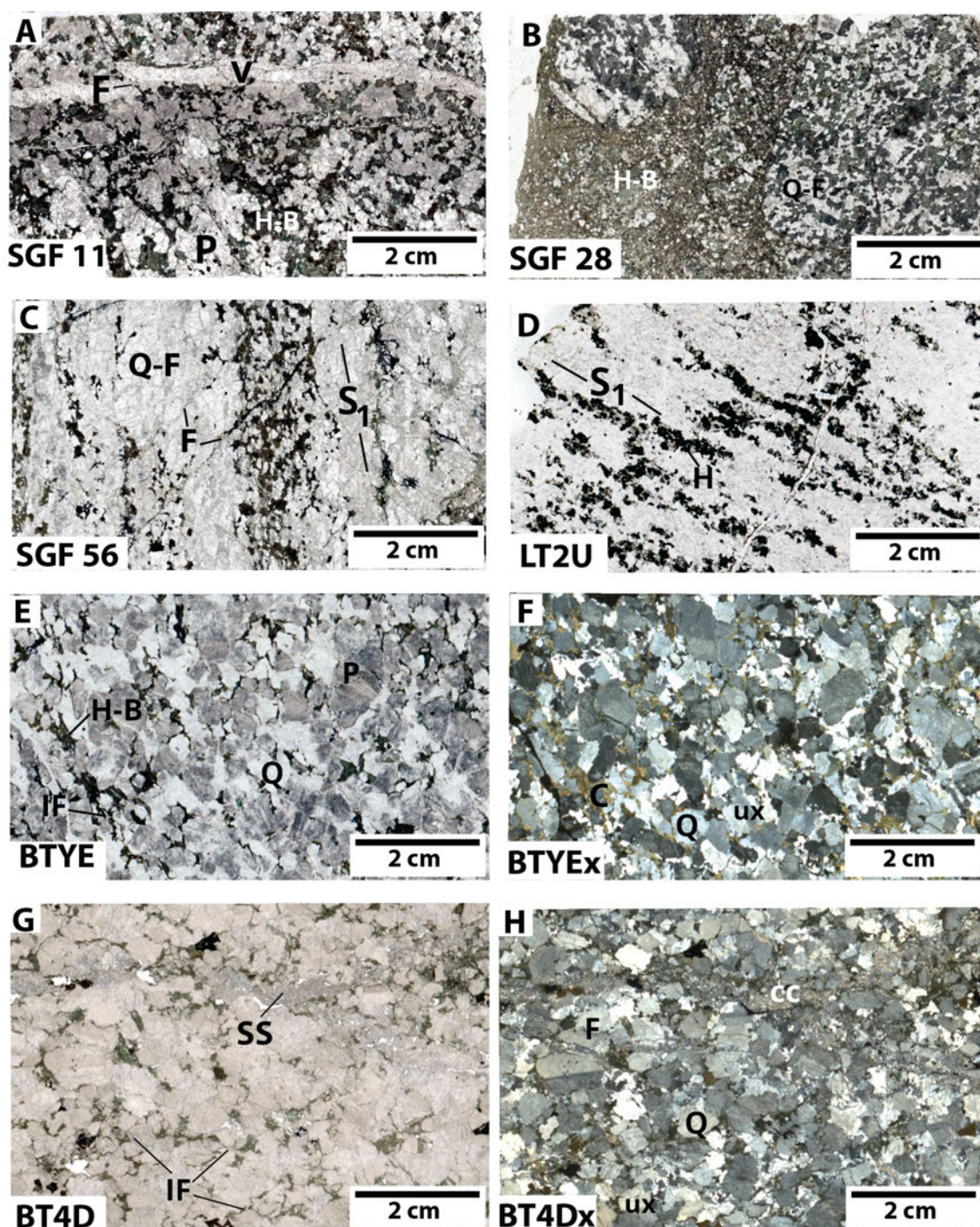


**Figure 9** – Images of whole thin sections of protolith sampled in core and outcrop. **(A)** Plane-polarized image of sample SGF 11 from the Mendenhall Gneiss on the north side of the fault. Moderately foliated quartz-feldspar-hornblende gneiss cut by quartz vein (V) and which exhibits equant quartz grains and alteration of hornblende to fine-grained biotite/chlorite (H-B). Coarse gneissic foliation is cut by small faults (F) and fracture systems. Plagioclase grains (P) contain numerous intragranular fractures. **(B)** Cross-polarized image of sample SGF 28 illustrating fine-grained hornblende-biotite (H-B) and quartzofeldspathic (Q-F) gneiss. **(C)** Sample SGF 56, a well-foliated ( $S_1$ ) quartz-feldspar-hornblende gneiss in which elongate quartz-feldspar grains exhibit (Q-F) cut by thin transgranular fractures (F) that show some dark material along the fracture. **(D)** Thin section of Mendenhall Gneiss sample LT2U. Foliation ( $S_1$ ) is defined by thin hornblende-rich (H) layers. **(E)** Cross-polarized light photomicrograph of Josephine Granodiorite sample BTYE in the outer damage zone of the San Gabriel Fault at the Big Tujunga site 4 shows slightly deformed granodiorite, with equant quartz grains (Q), hornblende  $\pm$  biotite (H-B), and grayish altered plagioclase (P). Intragranular fractures (IF) connect the hornblende-biotite zones. **(F)** Cross-polarized image of quartz-rich gneiss sample BTYEx dominated by quartz grains (Q) with undulose extinction (ux) and choritically altered (C) mafic grains. **(G)** Plane-polarized light photomicrograph of sample BT4D of the Josephine Granodiorite that consists of blocky feldspars (F) that are cut by intergranular fractures (IF) parallel to the long axis of the image and by narrow slip surfaces (SS) that exhibit initial stages of grain-scale fractures. The intergranular fractures are lined by altered Fe-rich material. **(H)** Cross-polarized photomicrographic of sample BT4Dx. Pre-existing deformed quartz (Q) with undulose extinction (UX) defines a metamorphic foliation ( $S_1$ ) cut by thin incipient fault comprised of fine-grained cataclasite (CC) and transgranular fractures.



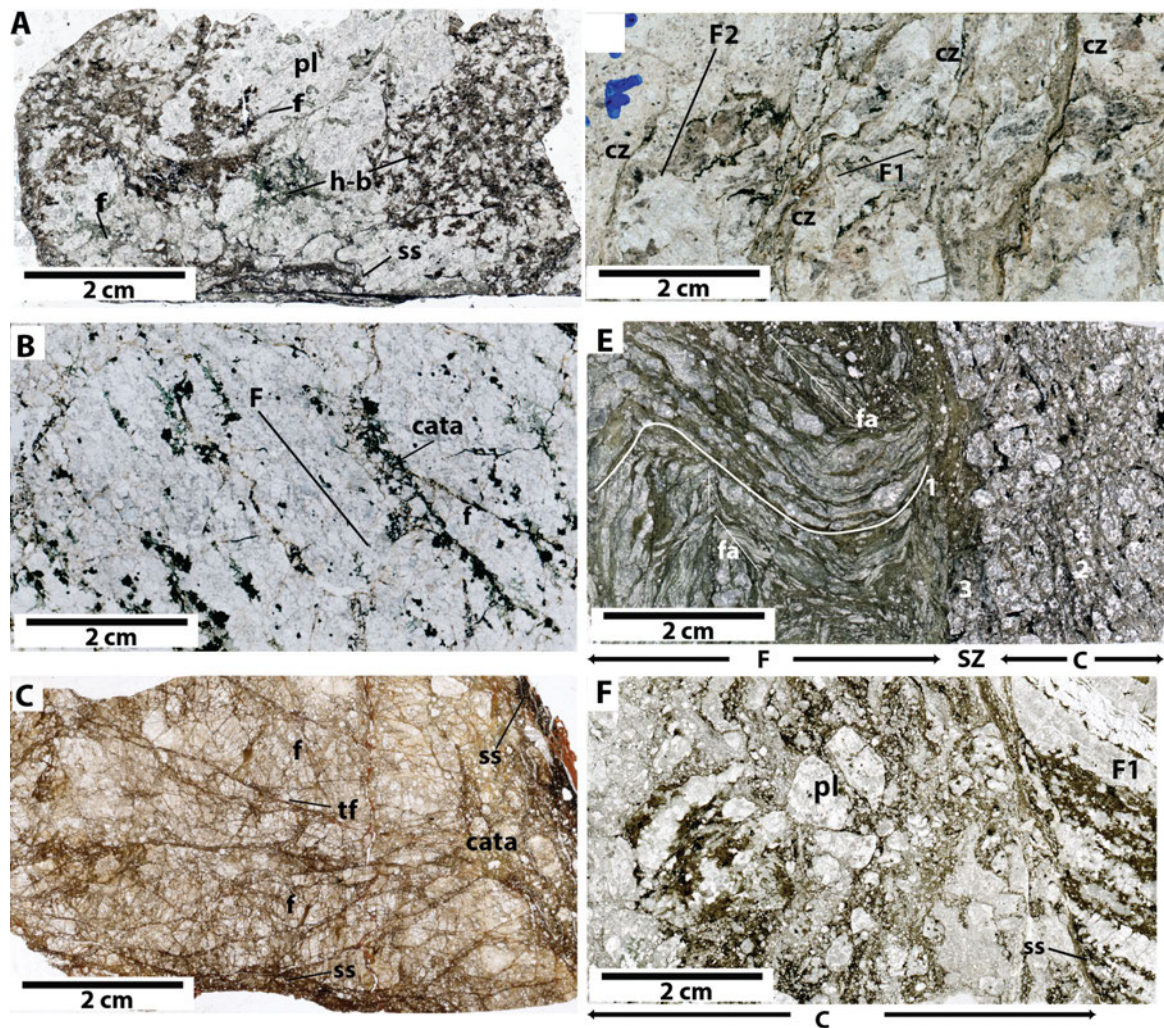


**Figure 10** – Images of whole thin sections of samples from the damage zones of the San Gabriel Fault in core and outcrop. **(A)** Microstructures in fractured Mendenhall Gneiss in the upper part of the ALT-B2 drill hole. Sample 39.2 ~120 m north of the upper fault zone consists of hornblende-biotite-rich zones (h-b), light-colored plagioclase-rich areas (pl), cut by fractures (f), and dark, thin slip surfaces (ss). **(B)** Sample LT2W from 1 m north of the main fault zone in plagioclase/amphibole gneiss. Plane-polarized light photomicrograph of sample LT2W of fractured Mendenhall Gneiss. Intragranular fractures (f) cut the sample at several orientations, including parallel to the foliation (F) demonstrating the initial stages of grain fragmentation and incorporation of alteration in the damage zone that leads to the development of early stages of cataclasite. **(C)** Plane-polarized light photomicrograph of Sample BT2B of damage zone adjacent to cataclasite in Josephine Granodiorite. Transgranular fractures (tf) and intragranular fractures (f) are marked by red-brown iron oxides, and the intragranular fractures form networks of angular fracture-bounded grains. The transgranular fractures appear to converge with a cataclasite zone (cata). Thin very fine-grained slip surfaces (ss) are composed of dark-brown to black ultracataclasite. **(D)** Plane-polarized light photomicrograph of sample LT2F from the south side of the fault zone in Josephine Granodiorite. Damage zone rocks exhibit steep dipping chloritic-clay shear zones (cz), with a flow-like fold fabric in places (F2) that cuts an earlier foliation (F1) defined by irregular shared biotite-hornblende zones (F1). **(E)** Cross-polarized light photomicrograph of Sample 60.1, from ~60 m north of the upper fault. Highly foliated zone (F – zone 1) consisting of chlorite-rich folia and carbonate-rich layers, separated from a cataclasite (C – zone 2) with a thin shear zone (sz – zone 3). Fold axes (fa) marked here indicate the location of some of the smaller folds in the carbonate-cataclasite sheared zone. **(F)** Plane-polarized light photomicrograph of sample 63-2m of protocataclasite (pc) that consists of angular to rounded plagioclase grains (pl) in deformed, fine-grained Fe-rich zones separated from the metamorphic foliations (F1) by a thin slip surface (ss).

The lower damage zone consists of highly sheared, altered, and mineralized rocks (Figure 13E). Cataclasites consist of quartz fragments in a matrix of fine-grained deformed feldspar fragments, with narrow black slip zones (Figure 13E). The lower principal fault zone is composed of extremely foliated and fine-grained gouge and cataclasite (Figure 13E) and ultracataclasite zones (Figure 13E), where dark, aphanitic sheared rock exhibits distinct

sharp boundaries between the zones.

Field samples provide examples of deformation of the Josephine Granodiorite and textures of alteration, mineralization, and shearing similar to those observed in the core samples (Supplemental File 6). The equigranular quartz-feldspar-biotite-amphibole granodiorite exhibits distributed zones of thin shear zones and distributed sheared gouge (Supplemental



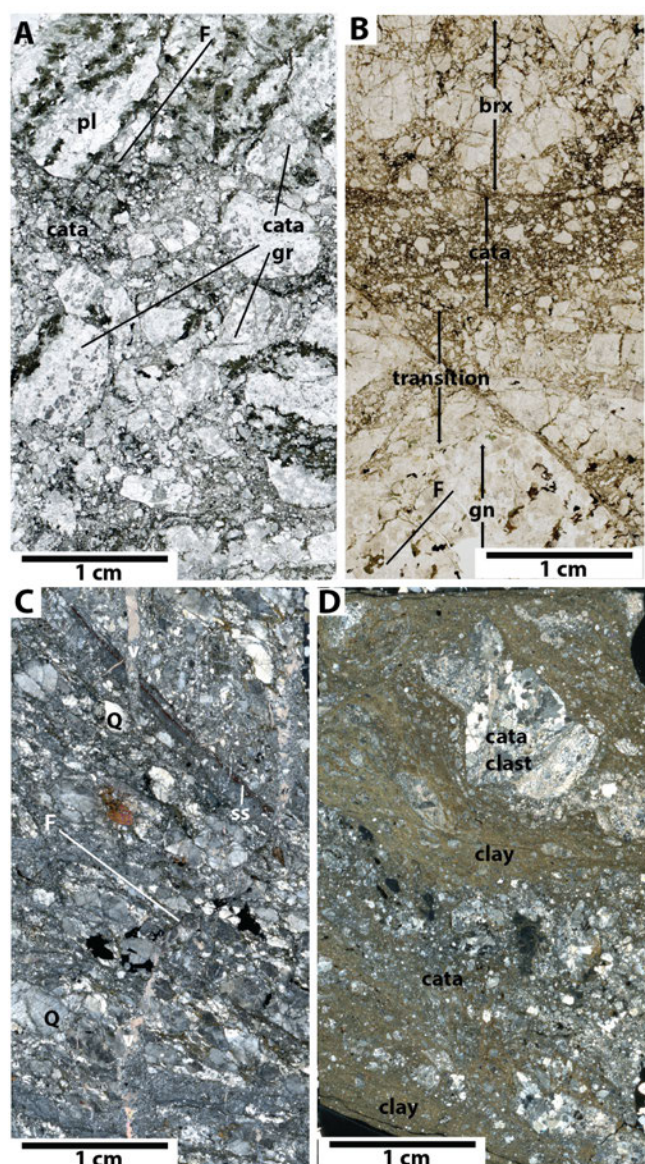


**Figure 11** – Images of whole thin sections that show examples of deformation, alteration, and mineralization from the damage zone of the San Gabriel fault. **(A)** Plane-polarized light photomicrograph of Sample LT 10BH. Remnants of the primary metamorphic foliation (F) are defined by elongated plagioclase grains (pl) and bands of hornblende ± biotite. Foliation is cut by a random fabric cataclasite composed of rounded cemented grains of cataclasite (cata gr) in a dark matrix. **(B)** Plane polarized photomicrograph of sample BT1C of cataclasite (cata) of angular feldspar fragments in a brown gouge matrix, bounded by a breccia (brx) comprised of grains with intragranular fracture, and a transition zone to primary gneiss (gn) with foliations F. **(C)** Cross-polarized photomicrograph of lithified/cemented cataclastically deformed sample SGF 92 with subrounded quartz grains (Q) in a matrix of altered feldspars that define a cataclastic foliation (F) cut by mm-scale slip surface (ss) and calcite veins (v). **(D)** Cross-polarized photomicrograph of sample 59C of highly sheared, foliated clay-rich cataclasite (cata). Earlier rounded grain of cemented quartzo-feldspathic (cata clast) is entrained in the clay-rich foliated zone.

File 6). Altered sheared cataclasite exhibits evidence of calcite mineralization, emplacement of zeolite veins, and grain-scale alteration (Figure 13F). Veins

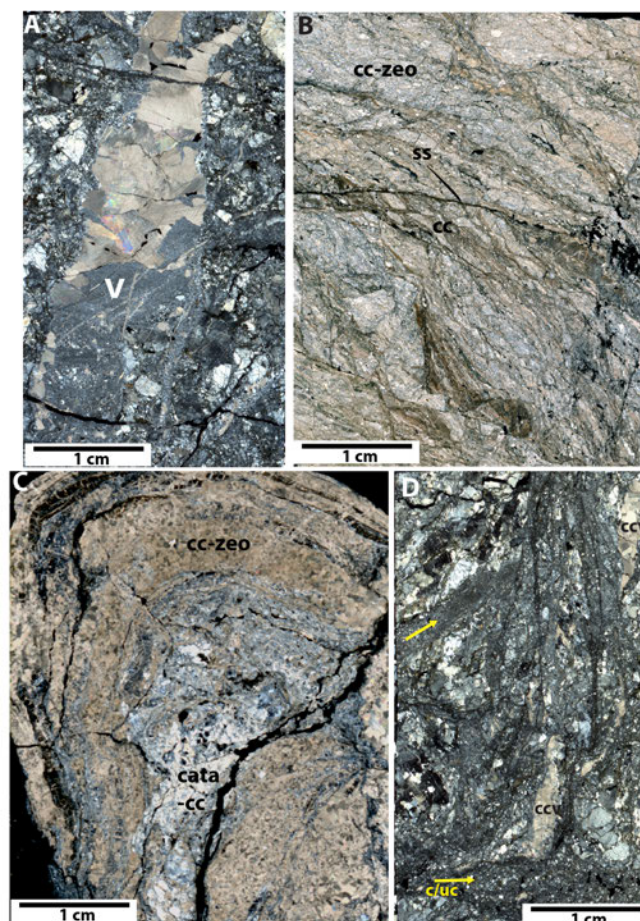


**Figure 12** – Images of whole thin sections that show examples of carbonate-zeolite mineralization in faulted rocks. **(A)** Cross-polarized photomicrograph of a thick, twinned calcite vein that cuts the cataclasite in sample SGF 95. **(B)** Cross-polarized photomicrograph of sample SGF 96.1 of carbonate (cc) lozenges and rounded clasts in a fine-grained matrix of alternating zones of carbonate ± zeolite (cc-zeo) and foliated cataclasite. A narrow slip surface (ss) or a solution seam cuts the sheared rock and is enhanced in Fe, Mn, Ni, and Cr (Evans *et al.*, 2023). The sample shows that carbonate ± zeolite mineralization developed in the fault zone and was subsequently sheared. **(C)** Cross-polarized photomicrograph of sample LT4DFH that shows layers of carbonate+zeolite (cc-zeo) and cataclasite with carbonate cement (cata-cc) in a tight fold, from 3 meters from the fault zone. **(D)** Cross-polarized photomicrograph of cataclastically deformed sample SGF 93.1 with vertical narrow slip surfaces (indicated by white arrows) that cut fine-grained cataclasite and calcite veins (CCV). These slip surfaces cut and are cut by cataclasite/ultracataclasite zones (c/uc).

are discrete, distributed, or large irregular zones. Highly sheared layers of altered cataclasite and sheared carbonate-zeolite veins are common. The rocks exhibit evidence for the development of several generations of finely foliated, iron-oxide-rich sheared rocks, that cut clasts of older clay-rich sheared rocks.

### 3.4 Mineralogy

The X-Ray diffraction analyses of the borehole samples (Table 2; Supplemental File 7) document



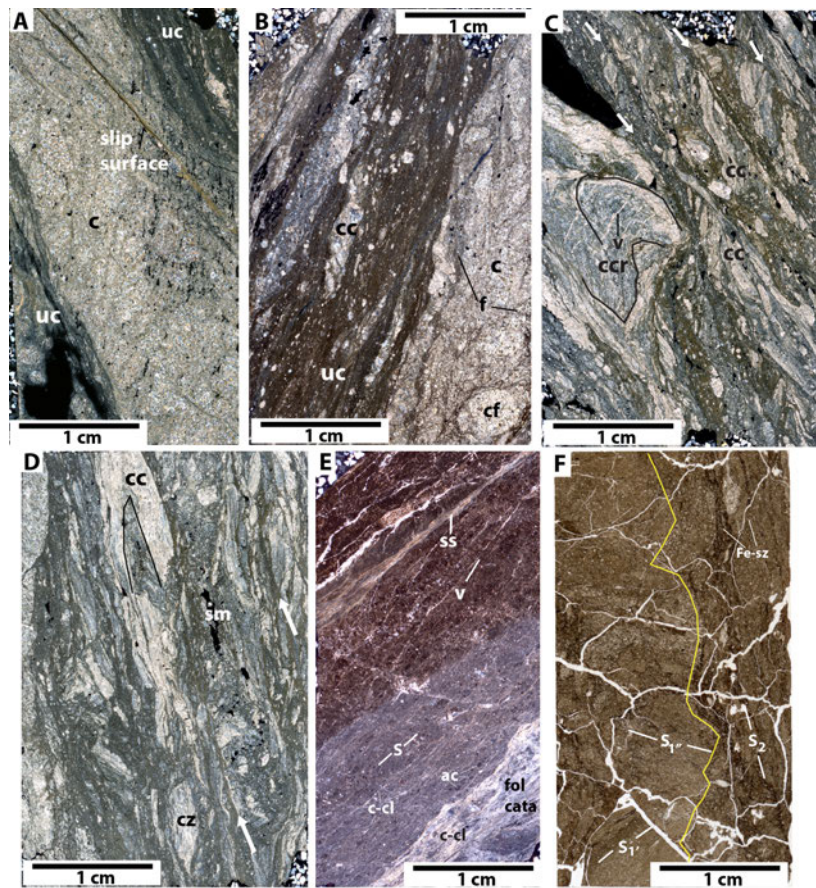


**Figure 13** – Images of portions of whole thin sections that show examples of highly sheared rocks from the principal slip surfaces of the San Gabriel Fault. **(A)** Cross-polarized light photomicrograph of sample SGF 103 of ultracataclasites (uc) bounded by cemented cataclasite (c), and an extremely thin slip surface. **(B)** Fine-grained foliated ultracataclasite (uc) in sample SGF 107, with a faint foliation with thin carbonate fragments (cc). Adjacent lithified cataclasite (c) is cut by healed fractures (f) and small faults and rounded fragments of older cataclasite (cf). **(C)** Highly sheared rock in sample SGF 65A from the north side of the upper fault zone in the ALT-B2 borehole. The sample displays numerous narrow slip surfaces, indicated by white arrows, that cut elongated calcite-zeolite fragments (cc). A large carbonate “roll” (CCR) consists of folded carbonate layers, indicated by the black lines, cut by later straight veins (v). **(D)** Sheared cataclasite in the upper slip zone from sample 65B with mm-wide slip surfaces marked by white arrows that cut fragmented angular and rootless folded carbonate grains (cc) that are subparallel to the slip surfaces. The fine-grained matrix of the sheared matrix (sm) contains angular fragments of carbonate-zeolite fragments (cz). **(E)** Ultracataclasite sample from the lower slip zone in sample SGF103. Different hues mark different textures in foliated cataclasites cut by narrow slip surfaces (ss). The slip surface is an mm-wide surface in dark brown (clay-rich?) cataclasite cut by thin carbonate veins (v). The dark gray zone consists of a foliated cataclasite defining a foliation (S) that contains small angular clasts (ac) and high birefringent carbonate-clay coated surfaces (c-cl). Lighter-colored foliated cataclasite consists of anastomosing fine-grained clay±carbonate zones (c-cl) that bound darker lozenges of less altered grains. **(F)** Cross-polarized light photomicrograph of sample BT4DF of highly sheared carbonate-zeolite ultracataclasite from field exposure. Dark-brown cataclasite/ultracataclasite with evidence of several episodes of deformation. Subvertical foliated cataclasite (S2) is marked by dark brown iron oxide-rich slip zones (Fe-sz) that cut an earlier foliated cataclasite (separated by the yellow line). The earlier cataclasite (S1' and S1'') is expressed as misoriented clasts separated by the white fractures.

the mineral assemblages in the protolith, damage zones, and principal slip zones. The Mendenhall Gneiss protolith consists of quartz, feldspar (albite and anorthite), amphibole, muscovite, biotite, and phlogopite. Unaltered mafic zones that consist of pyroxenes and plagioclase (Barth *et al.*, 1995b) are commonly altered to hornblende ± biotite ± calcite ± epidote ± quartz, and Mg- and Fe-oxide minerals. Due to the lack of unaltered granodiorite protolith samples in the ALT-B2 borehole, we rely on the work of Anderson *et al.* (1983) and Barth *et al.* (1995b) for primary mineralogy analyses.

The Josephine Intrusive suite rocks consist of

quartz, alkali feldspars, and lesser amounts of hornblende and biotite. Common alteration minerals in the upper damage zone consist of phlogopite, chlorite, calcite, and iron oxides. The upper principal slip zone includes calcite, clays (nontronite, glauconite), metal oxides (Fe and Mg, with traces of Zn, Sr, Mn), zeolites, and minor epidote. The lower damage zone contains laumontite, calcite, chloritic minerals, calcite, and clays (Table 1) and the lower principal slip zone exhibits Na-clays, micas, calcite, and zeolites.

**Table 2** – Summary of the X-Ray diffraction mineralogy analyses of samples showing major, minor, and present minerals. Sample locations are plotted in Figure 3 and sample details are in Supplemental File 7. DZ = damage zone; PSZ = principal slip zone.

Drill Core Run	Sample	Major Minerals	Minor Minerals	Present	Rock Type	Measured Depth (m)
11	11.2	Quartz, Albite	Muscovite, Biotite, Anorthite	± Sulfides	Protolith	55.9
28	28.2	Quartz, Albite	Zeolite, Actinolite		DZ	
39	39.1	Quartz	Albite	Phlogopite, ± sulfate	DZ	177.5
39	39.2	Quartz	Albite, Clay	Zeolites (laumontite), Mg oxide, ± Sr oxide?	DZ	177.5
49	49	Iron Oxide	Quartz, Nontronite, Albite, Mg Oxide	Calcite	DZ	223.2
51	51.2	Albite	Quartz, Calcite		DZ	229.5
51	51.3	Quartz, Albite	Biotite, Anorthite	Clay, ± Fe oxide	DZ	229.5
54	54.2	Quartz	Albite, Calcite	Muscovite, ± K-Mn Oxide	DZ	229.5
54	54.3	Quartz, Analcime	Albite	Zeolite , Mg-Fe silicate and oxide	DZ	244.4
56	56	Quartz, Albite, Phlogopite	Biotite	± Na-Al Silicate	Protolith	251
60.1	60.1-1	Quartz, Clay	Chloritic-serpentine, Biotite, Muscovite		DZ	267.3
60.1	60.1-2	Quartz	Albite, Phlogopite	Clay, ± Phosphate	DZ	267.3
60.2	60.2	Quartz	Albite	Phlogopite	Protolith	269.8
63	63-1	Quartz	Albite, Phlogopite		Protolith	281.6
63	63-2	Quartz	Albite		Protolith	281.6
64	64	Quartz	Mg-Mn Silicate	Biotite, Albite, Phlogopite	Protolith	287.9
65A	65A-1	Calcite	Quartz, Albite, Chloritic-serpentine	Clays	DZ	291.2
66	66.1	Quartz	Albite, Phlogopite, Biotite	± Epidote	DZ	295.9
66	66.2	Quartz	Albite-Ca	Orthoclase, ± Zircon	DZ	295.9
66	66.3	Quartz	Albite, Calcite		DZ	295.9
70	70-1	Quartz	Albite	Phlogopite	PSZ	314.6
71	71-1	Quartz	Albite, Calcite	± Mg oxide	PSZ	315.9
71	71-2	Quartz	Albite, glauconite	Calcite, Zeolite	PSZ	315.9
80	80.1	Quartz	Albite-Ca	Laumontite	DZ	360.7
80	80.2	Quartz	Albite	Laumontite	DZ	360.7
93.1	93.1	Quartz	Albite-Ca, zeolite (Co-Al phosphate)	Anorthite	DZ	413.3
93.2	93.2	Quartz	Albite-Ca, Orthoclase		DZ	413.5
93.3	93.3	Quartz	Albite, Calcite, Zeolite		DZ	416.3
94.2	94.2	Quartz	Albite-Ca-zeolite		DZ	418.9
96	96.1	Quartz	Albite-Ca, chloritic-serpentine calcite	± oxide, ± calcite/dolomite	DZ	426.3
96	96.2	Quartz	Calcite, Muscovite, Albite, Mica	Clay, Muscovite, Calcite, Mg oxide	DZ	426.3
103	103.1	Quartz	Clay, K-Na mica	Clay, zeolite (Na-Al silicate)	PSZ	456.4
103	103.2	Quartz, Albite	Anorthite, zeolite (Na-Al silicate)	Laumontite	PSZ	456.4
107	107.1	Quartz	Albite	Zeolite ± Cu-As sulfide	PSZ	472.3



## 4 Discussion

This analysis of the CHSRA ALT-B2 borehole across the North Branch of the San Gabriel Fault, and the results of related work (Anderson *et al.*, 1983; Chester *et al.*, 1993; Evans and Chester, 1995; Evans *et al.*, 2023), enables us to define the mesoscopic structure of the fault and the nature and relationships of the physical properties of fault-related rocks. The San Gabriel Fault zone comprises an ~200 m wide damage zone, with two principal slip zones of indurated cataclasite that mark areas of localized slip. The fault-related rocks in the damage zones are comprised of altered and mineralized rocks. Fault-related rocks in the principal slip zones and damage zones exhibit cross-cutting relationships among brittle and semi-brittle structures and mineralization features. We show that these geologic textures and compositional variations are manifest in borehole- and core-based observations of the engineering rock properties.

### 4.1 San Gabriel Fault Zone Structure

The data from the ALT-B2 borehole and nearby outcrops of the San Gabriel Fault document the presence of complexly deformed and altered rocks in the fault damage zones that encompass two principal slip zones (Figure 14). Fault slip likely focused on the upper 6.5 m thick principal slip zone (Figures 3, 14) at 313–325 m measured depth and an 11-m thick lower principal slip zone at 456.5–476.5 m measured depth. The upper fault is likely the down-dip continuation of the surface trace of the fault (Figures 5, 6), evidenced by the fault geometry, inclination of the borehole, the dip of the SGF, and juxtaposition of the host rock Mendenhall Gneiss and Josephine Granodiorite in the borehole (Figure 3; see also d'Alessio, 2004). The cataclasite samples in the 6.5 m thick upper principal slip zone match descriptions of the surface expression of the SGF, in which the principal slip zone, termed the fault core (Chester *et al.*, 1993; Evans and Chester, 1995), is an m-thick cataclasite and cm- to m-thick ultracataclasite.

Along strike and down dip, the structure of the San Gabriel Fault zone varies from a single fault zone with a narrow principal slip surface to multiple fault surfaces in sheared and damaged rocks. The steep fault zone varies from southward to northward dips across the region (Figure 5; Supplemental File 3; see also Anderson *et al.*, 1983; Dibblee and Ehrenspeck, 1991a,b; Dibblee and Carter, 2002; Yerkes and Campbell, 2005; Campbell *et al.*, 2014). The lower fault zone in the ALT-B2 borehole is likely a lower branch of the SGF that merges along the strike to form the single-stranded fault expressed to the northwest and southeast (Figure 2; Dibblee and Ehrenspeck, 1991a,b). The 11-m thick lower principal slip zone exhibits indurated clay fault gouge and ultracataclasite, suggesting fault maturity in the formation of these ultrafine-grained fault-related rocks. The penetrative ultracataclasite we document

is similar to those described in the SGF by Chester *et al.* (1993) and Evans and Chester (1995). We do not observe random fabric fault gouge with little or no cohesion in any of the rocks retrieved in the drill core nor outcrops.

The total width of the fault zone recorded by the rocks retrieved in borehole ALT-B2 is nearly 200 m, with ~60 m on the north side of the SGF and ~50 m between the two principal slip zones. An unknown amount of damage zone extends below the lower extent of the borehole; the lower principal slip zone could therefore be embedded within a total damage zone that exceeds 100 m wide. The presence of indurated clay-rich gouge, foliated cataclasite, and well-developed ultracataclasite, and the nature of hydrothermal alteration in the lower fault zone (see Section 4.2), suggests the lower fault zone may be the mature strand here and may have been responsible for a significant fraction of overall slip. Dibblee and Ehrenspeck (1991b) show the De Mille Fault (Weber, 1982), a Quaternary to late Tertiary fault that forms the southern boundary of an ~10 km long, up to 1.4 km wide fault zone, bounded by the San Gabriel Fault (*sensu stricto*) on its northern side. The upper, northeastern fault encountered in the ALT-B2 borehole may be the subsurface expression of the northern strand of the fault, whereas the lower, southwestern fault zone encountered in the borehole may correlate with the DeMille Fault, as mapped by Dibblee and Ehrenspeck (1991a), where it merges with the San Gabriel Fault in the region of the borehole.

The ~50 m thick damage zone between the two principal slip zones exhibits extremely low RMR1989 values (Figure 14), intense deformation, and slightly less induration than the highly fractured and sheared sections of Mendenhall Gneiss damage zone north of the upper trace of the SGF. Mesoscopic fractures and veins in the Josephine Granodiorite damage zone south of the SGF are up to 1.5 cm wide and >20 cm long, suggesting variances in fluid-rock interaction throughout the SGF. The highly sheared fault-related rocks in the drill core contain lozenges of protocataclasite of the gneissic damage zone directly north of the principal slip zone (Figures 3–5, 7–9). These rocks transition toward the lower principal slip zone where shearing is highly localized (Figure 7D, F). Damaged and altered rocks within these lower fracture intensity zones exhibit multiple generations of folds and re-folds of cataclasites, implying that simple shear deformation occurred (Figure 11C) in the gneisses. These fabrics were perhaps due to the composition of the gneissic protolith, where fracture linkage and shearing were facilitated between the layered silicates (c.f., Borg and Handin, 1966; Evans, 1990) and alteration in the Fe- and Mg-bearing minerals (Evans and Chester, 1995).

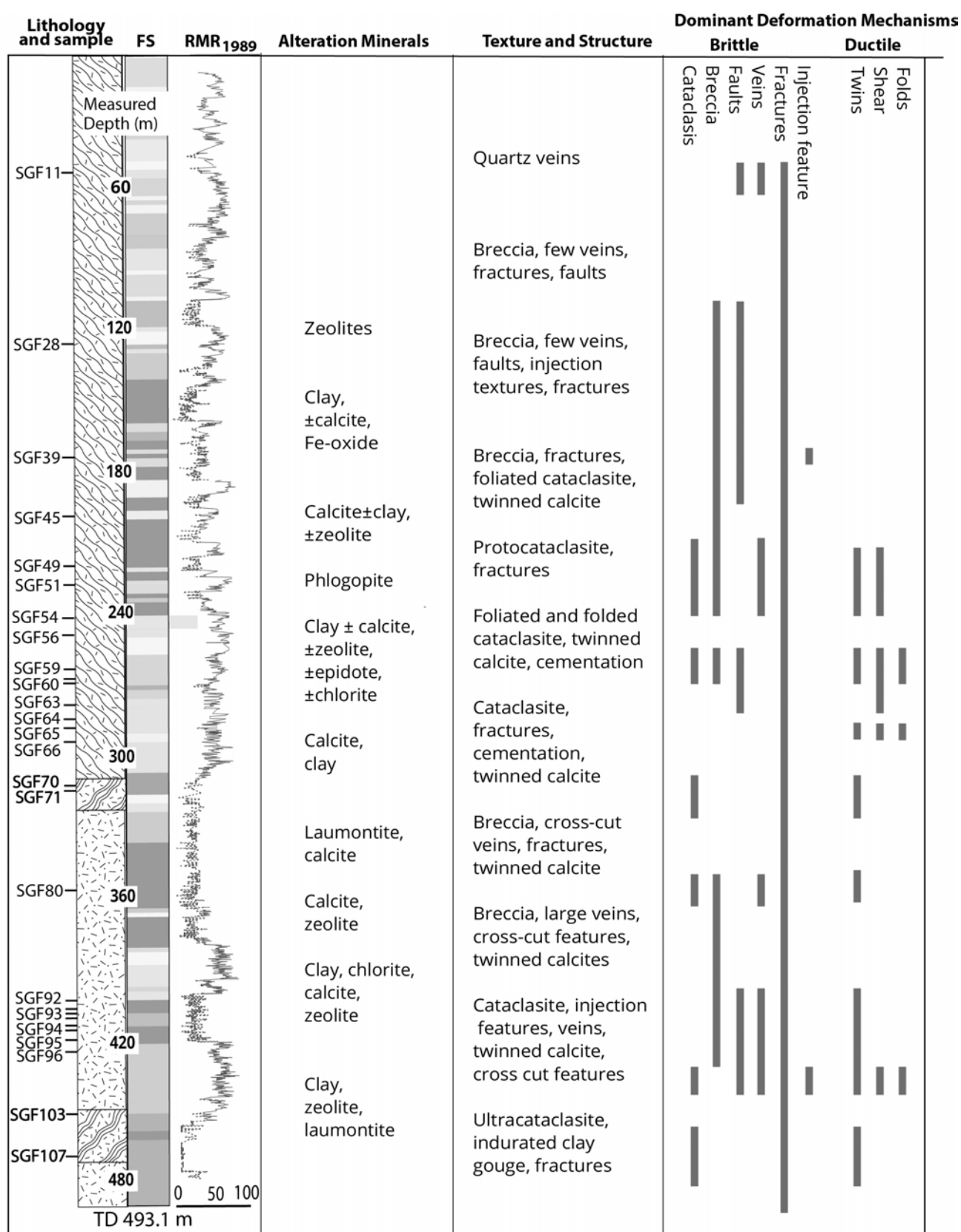


**Figure 14** – Summary interpretation of the San Gabriel Fault zone sampled by the ALT-B2 borehole. The data consist of primary lithologies, fracture spacing, RMR1989 data from core logging data (Supplemental Files 2 and 8), and summaries of microstructural and mineralogical analyses of the ALT-B2 core across the San Gabriel Fault, southern California. Whole-rock geochemical analyses and textural data are from the work shown here, based on X-Ray Fluorescence mapping using a synchrotron radiation lightsource (Evans *et al.*, 2023). The narrow slip surface at 310 m has a damage zone above it and is characterized by the presence of clay minerals, zeolite, and epidote, high values of loss on ignition geochemical concentrations, and the presence of cataclasites. The damage zones are marked by very low to low RMR values, which are due to high fracture densities, the increased presence of alteration minerals including calcite, zeolites, and clays.



## 4.2 Fault Rock Composition, Textures, and Mechanisms

The fault-related rocks in the San Gabriel Fault indicate that significant amounts of fluid-assisted alteration occurred within the fault zone. Zeolites, calcite in intragranular cement and in veins, epidote, chlorite, and a range of clays formed in samples that span the length of the borehole (Table 1). The Fe- and Mg-rich phyllosilicates in the principal slip zones and fault-related rock and sheared gneiss include nontronite (Fe-rich smectite), chlorite-serpentine, and glauconite. The clay and phyllosilicate minerals are constrained to the principal slip zones and the zones of shearing directly north of the principal slip zones (Figures 4D-F, H; 7F-I; Table 1).

The microtextures documented here, and the whole-rock geochemistry of the deformed rocks sampled by the ALT-B2 borehole (Evans *et al.*, 2023) and in the field at the surface (Evans and Chester, 1995), indicate that significant fluid-rock interactions occurred in these rocks. Cementation and fluid mineralization within the fractured and brecciated rock suggest that the SGF experienced post-seismic healing, evidenced by the textures of the breccia matrix (Figure 11) and calcite and chlorite veins. Due to the widespread evidence for fluid-rock interactions, we suggest that fluid-assisted processes contribute to grain-scale brittle fault processes and shearing and folding within clay-rich and carbonate-zeolite zones in the shallow SGF.

Calcite and Ca-bearing zeolites in the damage zone are present as discrete veins and disseminated grains, with little to no elemental mixing in slip surfaces, breccia matrices, and shear fabrics (Figure 13). This suggests that the precipitation of Ca differs mechanically and concomitantly from the concentration and mineralization of other elements in the system. Cross-cutting relationships of veins, fractures, folds, and sheared rocks indicate that the SGF experienced altering cycles of slip energy followed by post-slip mineralization and healing. The mineralization represented by the chlorite-zeolite assemblages and alteration of the damaged rocks due to hydrothermal processes resulted in the development of sharp, concentrated slip surfaces and cataclasite observed in the fault-damaged rock.

The presence of well-indurated fault-related rocks at such shallow depths is inconsistent with fault-zone models that postulate that the upper several kilometers of faults consist of unconsolidated to poorly consolidated gouge or breccia, clay gouge, or pulverized rocks (Figure 1; *c.f.*, Woodcock and Mort 2008; Scholz 2019). Cohesive, mineralized, and 'cemented' cataclasite and intact fault gouge developed in the upper 2-3 km of this major fault zone. The textures and alteration patterns in fault-related rocks of the SGF and the estimates of rock properties (Table 2; Figure 14) indicate that the majority of slip is localized to the principal slip zones as documented by the fine- and ultrafine-grained

deformed rocks of cataclasite, clay gouge, and ultracataclasite (Chester *et al.*, 1993; Evans and Chester, 1995; Chester and Chester, 1998). The presence of weak phyllosilicate and clay minerals (Warr and Cox, 2001; Haines *et al.*, 2009; Schleicher *et al.*, 2012), shear fabrics, folds, and numerous fractures and faults in the sheared zones next to the principal slip zones provide evidence for multiple generations of folding, cataclasite development, and vein formation, indicating prolonged or repeated episodes of distributed deformation. Rootless and elongated calcite lozenges in sheared material indicate the systematic shearing of altered fault-related rock. Twinned calcite recorded here in the SGF (Figure 11) occurs in low temperatures due to crystal-plastic deformation mechanisms (Barber and Wenk, 1979; Rowe and Rutter, 1990; Ferrill *et al.*, 2004).

Evidence for complex overprinting of grain-scale brittle and distributed shearing fabrics lies in the presence of folded cataclasites and twinned calcite in veins juxtaposed against and within fault breccias (Figure 13). This pattern of overprinting indicates a complex history that includes the formation of cataclasite, the reworking and folding of cataclasite, the formation of new breccia and cataclasites, and the truncation of the folded cataclasite and breccia by slip surfaces and veins. The pervasiveness and cross-cutting nature of alteration and deformation textures recorded throughout the SGF reveal a complex interplay and overprinting of mechanisms during faulting. This is consistent with other analyses of fault-related rocks that formed at 2-4 km depth in the San Andreas Fault system (Chester and Logan, 1986; Schulz and Evans, 1998, 2000; Schleicher *et al.*, 2009, 2012; Holdsworth *et al.*, 2011; Bradbury *et al.*, 2015; Forand *et al.*, 2018; Studnický, 2021), the San Gabriel Fault (Anderson *et al.*, 1983; Chester *et al.*, 1993; Evans and Chester, 1995; Chester and Chester, 1998), and other faults (Bruhn *et al.*, 1994; Gratier *et al.*, 2003; Faulkner *et al.*, 2003; Wibberley and Shimamoto, 2003; Marone and Saffer, 2007; Wibberley *et al.*, 2008; Mitchell and Faulkner, 2009; Rutter *et al.*, 2012; Boulton *et al.*, 2017). These distributed fault- and shear-zone zones are produced by complex interactions of deformation, alteration, and mineralization within these zones (Blenkinsop *et al.*, 2020).

## 4.3 Utility of Geotechnical Investigations

One of the important outcomes of this and related work (Williams *et al.*, 2021; Studnický, 2021; Evans *et al.*, 2023) is that we show that mission-driven drilling projects investigating subsurface geology that may, at first glance, not be related to fundamental science can yield a range of high-quality data that can be used to address scientific questions. Studies of the subsurface geology and rock properties acquired from coring, especially studies in which public funding results in open access to data and samples, provide samples and data that would be prohibitively expensive for scientific research groups.

The subsurface analyses in these studies are often performed to a range of engineering standards, are well documented, and are internally and externally reviewed for quality and content.

## 5 Conclusions

The macroscopic to microscopic deformation and alteration patterns in fault-related rocks of the San Gabriel Fault show that the damaged zones of the upper San Gabriel Fault document the interplay of deformation and alteration of the rocks. This alteration, marked by the development of clays, zeolite minerals, and calcite, and the geochemical variations (Figure 14), marks the presence of the damage. We suggest the majority of coseismic slip is localized to the principal slip zones as documented by the fine- and ultrafine-grained deformed rocks of cataclasite, clay gouge, and ultracataclasite (Chester *et al.*, 1993; Evans and Chester, 1995). The folded and layered cataclasite textures in the clay-rich fault-related rock likely formed in the rock's systematic shearing and aseismic deformation. Evidence for multiple generations of folding, cataclasite development, and vein formation indicates prolonged periods of deformation. Rootless and elongated calcite lozenges in plastically sheared material are indicators for the shearing of altered fault-related rock.

We show microstructural and mineralogic evidence of overprinted deformation and alteration (Figure 14). We infer that alteration and hydrothermally induced mechanisms are integral in shallow fault processes and should be accounted for in fault and earthquake models. This is supported by analyses of fault-related rocks that formed at 2-3 km depth in the San Andreas Fault (Studnicky, 2021), the San Gabriel Fault (Anderson *et al.*, 1983), and other faults that recorded similar results (Gratier *et al.*, 2003; Faulkner *et al.*, 2003; Jefferies *et al.*, 2006; Marone and Saffer, 2007; Mitchell and Faulkner, 2009; Holdsworth *et al.*, 2011; Rutter *et al.*, 2012; Bradbury *et al.*, 2015; Boulton *et al.*, 2017; Williams *et al.*, 2021)

Our results for a cored section of the exhumed San Gabriel Fault document the nature of deformation mechanisms, alteration, fluid-rock interactions, and the mesoscopic structure of the fault. Our results, along with other studies (Ohtani *et al.*, 2000; Zoback *et al.*, 2010; Boullier, 2011; Sutherland *et al.*, 2012; Duan *et al.*, 2016) support a model of fault zones that consists of narrow slip surfaces embedded in damage zones with reduced strength relative to the host rock (c.f., Roten *et al.*, 2017b). These data constrain models of earthquake hazards, seismic energy dissipation, and long-term seismic behavior (Kaneko and Fialko, 2011; Huang *et al.*, 2014; Roten *et al.*, 2017a; Thakur *et al.*, 2020). Our data records pervasive and cross-cutting brittle and distributed deformation textures, indicating influence from seismic and aseismic deformation mechanisms within the deformed and altered shallow San

Gabriel Fault. These data document the need to consider both mechanisms when modeling fault and earthquake behavior over the entire depth range of fault zones. Observations and data quantification made here on the SGF may serve as an analog to help decipher the nearby active San Andreas fault and similar faults.

## Acknowledgements

This work was funded by NSF grants EAR-920577 and 1824852, SCEC grant 18077, and USGS-NEHRP grant 1434-92-G-2184 to Evans. Grants from the Geological Society of America - Continental Scientific Drilling Division, American Association of Petroleum Geologists L. Austin Weeks grant, a Utah State University Academic Opportunity, URCO, Peak Summer Research Fellowship, and a College of Science grant supported Kaitlyn Crouch. Many thanks to Caroline Studnicky for the initial collection of core samples, to Kathleen Red (Kleinfelder) and Randy Anderson (CHSRA) for help accessing the core in 2019, and to Paul Gupitill (Kleinfelder) and the California High-Speed Rail Authority for accessing data from the borehole released under the California High-Speed Rail Public Records request # 22-164. Field data, sample collection, and outcrop photos by Jonathan Caine, David Forand, and Joseph Jacobs, and photography of samples by Roxie Crouch are gratefully acknowledged. Steven Schulz prepared some of the field samples for the thin-section study. Reviews of earlier versions of this paper by Susanne Jänecke and the UW-Madison Structure and Tectonics group helped to greatly improve the manuscript. Many thanks to journal reviewers, Ben Melosh and two other reviewers for thoughtful reviews of this paper, and to journal editors Janine Kavanagh and Jack Williams for their editorial efforts.

## Author contributions

**Evans** conceptualized this project, designed the methodologies, sampled the core in 2019, and revised, reviewed, and edited the current draft of this paper. **Crouch** sampled the core, and conducted most of the research, including examining the core in detail, compiling the fracture spacing and RMR data from the borehole data, performed the microstructural studies, examined and interpreted the thin sections, performed the X-Ray diffraction studies, and compiled and curated all of the data sets. She wrote the original draft of this work. Together **Crouch and Evans** synthesized and interpreted the data for this paper.

## Data availability

Supplemental files 1, 4, 5, 6, and 7 can be found at [https://digitalcommons.usu.edu/all\\_datasets/193/](https://digitalcommons.usu.edu/all_datasets/193/). Supplemental files 2, 3, and 8 can be found in the [Supporting Information](#) attached to this paper. The



original data from the geotechnical investigation of the core, rock quality data, fracture data, and related analyses are contained in: Preliminary Geotechnical Data Report for Tunnel Feasibility, Angeles National Forest, California High-Speed Rail Authority, Palmdale to Burbank Project Section, 2019. These data were released to us under request 22-164 filed on September 14, 2022, and fulfilled September 26, 2022, via the High Speed Rail Authority Public Record Act Portal: <https://hsr-ca.nextrequest.com>. These data can be requested by any person or group via the data portal, and the report number is: EEPB-KLF-TK04-RE-0006\_REV01 ANF PGDR.

## Competing interests

The authors declare no competing interests.

## Peer review

This publication was peer-reviewed by Benjamin Melosh and two anonymous reviewers. The full peer-review report can be found here: [tektonika.online/index.php/home/article/view/30/44](https://tektonika.online/index.php/home/article/view/30/44)

## Copyright notice

© Author(s) 2023. This article is distributed under the [Creative Commons Attribution 4.0 International License](https://creativecommons.org/licenses/by/4.0/), which permits unrestricted use, distribution, and reproduction in any medium, provided the original author(s) and source are credited, and any changes made are indicated.

## References

- Allmendinger, R. W., N. Cardozo, and D. M. Fisher (2011), *Structural Geology Algorithms: Vectors and Tensors*, Cambridge University Press.
- Anderson, J. L., R. H. Osborne, and D. F. Palmer (1983), Cataclastic rocks of the San Gabriel fault—an expression of deformation at deeper crustal levels in the San Andreas fault zone, *Tectonophysics*, 98(3-4), 209–251, doi: 10.1016/0040-1951(83)90296-2.
- Aydan, Ö., R. Ulusay, and N. Tokashiki (2014), A new rock mass quality rating system: Rock mass quality rating (RMQR) and its application to the estimation of geomechanical characteristics of rock masses, *Rock Mechanics and Rock Engineering*, 47(4), 1255–1276, doi: 10.1007/s00603-013-0462-z.
- Barber, D. J., and H.-R. Wenk (1979), Deformation twinning in calcite, dolomite, and other rhombohedral carbonates, *Physics and Chemistry of Minerals*, 5(2), 141–165, doi: 10.1007/BF00307550.
- Barth, A. P., and P. L. Ehlig (1988), Geochemistry and petrogenesis of the marginal zone of the Mount Lowe Intrusion, central San Gabriel Mountains, California, *Contributions to mineralogy and petrology. Beitrage zur Mineralogie und Petrologie*, 100(2), 192–204, doi: 10.1007/BF00373585.
- Barth, A. P., J. L. Wooden, R. M. Tosdal, and J. Morrison (1995a), Crustal contamination in the petrogenesis of a calc-alkalic rock series: Josephine Mountain intrusion, California, *GSA Bulletin*, 107(2), 201–212, doi: 10.1130/0016-7606(1995)107<0201:CCITPO>2.3.CO;2.
- Barth, A. P., J. L. Wooden, R. M. Tosdal, J. Morrison, D. L. Dawson, and B. M. Hernly (1995b), Origin of gneisses in the aureole of the San Gabriel anorthosite complex and implications for the Proterozoic crustal evolution of southern California, *Tectonics*, 14, 736–752, doi: 10.1130/0016-7606(1995)107<0201:CCITPO>2.3.CO;2.
- Beyer, L. A., T. H. McCulloh, R. E. Denison, R. W. Morin, R. J. Enrico, J. A. Barron, and R. J. Fleck (2009), Post-Miocene right separation on the San Gabriel and Vasquez Creek faults, with supporting chronostratigraphy, western San Gabriel Mountains California, *Tech. rep.*, U.S. Geological Survey.
- Bieniawski, Z. T. (1989), *Engineering rock mass classifications: A complete manual for engineers and geologists in mining, civil, and petroleum engineering*, 250 pp., John Wiley & Sons, Nashville, TN.
- Bieniawski, Z. T. (1993), 22 - Classification of Rock Masses for Engineering: The RMR System and Future Trends, in *Rock Testing and Site Characterization*, edited by J. A. Hudson, pp. 553–573, Pergamon, Oxford, doi: 10.1016/B978-0-08-042066-0.50028-8.
- Blenkinsop, T. G., N. H. S. Oliver, P. G. H. M. Dirks, M. Nugus, G. Tripp, and I. Sanislav (2020), Chapter 1: Structural Geology Applied to the Evaluation of Hydrothermal Gold Deposits, in *APPLIED STRUCTURAL GEOLOGY OF ORE-FORMING HYDROTHERMAL SYSTEMS*, Society of Economic Geologists, doi: 10.5382/rev.21.01.
- Blythe, A. E., M. A. House, and J. A. Spotila (2002), Low-temperature thermochronology of the san gabriel and san bernardino mountains, southern california: Constraining structural evolution, in *Contributions to Crustal Evolution of the Southwestern United States*, edited by A. Barth, Special Paper, pp. 231–250, Geological Society of America, doi: 10.1130/0-8137-2365-5.231.
- Borg, I., and J. Handin (1966), Experimental deformation of crystalline rocks, *Tectonophysics*, 3(4), 249–367, doi: 10.1016/0040-1951(66)90019-9.
- Boullier, A.-M. (2011), Fault-zone geology: lessons from drilling through the Nojima and Chelungpu faults, <https://www.lyellcollection.org/doi/10.1144/SP359.2>, doi: 10.1144/SP359.2, accessed: 2023-9-15.
- Boulton, C., C. D. Menzies, V. G. Toy, J. Townend, and R. Sutherland (2017), Geochemical and microstructural evidence for interseismic changes in fault zone permeability and strength, Alpine Fault, New Zealand, *Geochemistry, Geophysics, Geosystems*, 18(1), 238–265, doi: 10.1002/2016gc006588.
- Bradbury, K. K., C. R. Davis, J. W. Shervais, S. U. Janecke, and J. P. Evans (2015), Composition, Alteration, and Texture of Fault-Related Rocks from Safod Core and Surface Outcrop Analogs: Evidence for Deformation Processes and Fluid-Rock Interactions, *Pure and Applied Geophysics*, 172(5), 1053–1078, doi: 10.1007/s00024-014-0896-6.
- Bruhn, R. L., W. T. Parry, W. A. Yonkee, and T. Thompson (1994), Fracturing and hydrothermal alteration in normal fault zones, *Pure and Applied Geophysics*, 142(3), 609–644, doi: 10.1007/BF00876057.
- Bryant, W. A. (2017), Fault number 89c, San Gabriel fault zone, Newhall section, in Quaternary fault and fold database of the United States, <https://earthquake.usgs.gov/static/lfs/nshm/qfaults/Reports/89c.pdf>.

- Bull, W. B. (1978), South Front of the San Gabriel Mountains, southern California, Final Technical report, *Tech. rep.*, U.S. Geological Survey.
- Caine, J. S., J. P. Evans, and C. B. Forster (1996), Fault zone architecture and permeability structure, *Geology*, 24(11), 1025–1028, doi: 10.1130/0091-7613(1996)024<1025:FZAAPS>2.3.CO;2.
- Callahan, O. A., P. Eichhubl, and N. C. Davatzes (2020), Mineral precipitation as a mechanism of fault core growth, *Journal of Structural Geology*, 140, 104,156, doi: 10.1016/j.jsg.2020.104156.
- Caltrans (2010), *Soil and Rock Logging, Classification, and Presentation Manual*, California Department of Transportation, Division of Engineering Services, Geotechnical Services.
- Campbell, R. H., C. J. Wills, P. J. Irvine, and B. J. Swanson (2014), Preliminary Geologic Map of the Los Angeles 30' x 60' Quadrangle, California Version 2.0, *Tech. rep.*, California Geological Survey.
- Cardozo, N., and R. W. Allmendinger (2013), Spherical projections with OSXStereonet, *Computers & geosciences*, 51, 193–205, doi: 10.1016/j.cageo.2012.07.021.
- Chen, K. H., and R. Bürgmann (2017), Creeping faults: Good news, bad news?, *Reviews of Geophysics*, 55, 282–286, doi: 10.1002/2017RG000565.
- Chester, F. M., and J. S. Chester (1998), Ultracataclastic structure and friction processes of the Punchbowl fault, San Andreas system, California, *Tectonophysics*, 295(1), 199–221, doi: 10.1016/S0040-1951(98)00121-8.
- Chester, F. M., and J. M. Logan (1986), Implications for mechanical properties of brittle faults from observations of the Punchbowl fault zone, California, *Pure and Applied Geophysics*, 124(1), 79–106, doi: 10.1007/BF00875720.
- Chester, F. M., J. P. Evans, and R. L. Biegel (1993), Internal structure and weakening mechanisms of the San Andreas Fault, *Journal of Geophysical Research, [Solid Earth]*, 98(B1), 771–786, doi: 10.1029/92JB01866.
- d'Alessio, M. A. (2004), The thermal and mechanical behavior of faults, Ph.D. thesis, University of California, Berkeley, Ann Arbor, United States.
- Dibblee, T. W., Jr, and B. Carter (2002), Geologic Map of the Condor Peak Quadrangle, Los Angeles, CA, *Tech. rep.*, Dibblee Foundation.
- Dibblee, T. W., Jr, and H. E. Ehrenspeck (1991a), Geologic Map of the Sunland and North Burbank Quadrangles, Los Angeles, CA, *Tech. rep.*, Dibblee Foundation.
- Dibblee, T. W., Jr, and H. E. Ehrenspeck (1991b), Geologic map of the San Fernando and Van Nuys (north half) quadrangles, Los Angeles County, California, *Tech. rep.*, Dibblee Foundation.
- Dolan, J. F., and B. D. Haravitch (2014), How well do surface slip measurements track slip at depth in large strike-slip earthquakes? the importance of fault structural maturity in controlling on-fault slip versus off-fault surface deformation, *Earth and planetary science letters*, 388, 38–47, doi: 10.1016/j.epsl.2013.11.043.
- Duan, Q., X. Yang, S. Ma, J. Chen, and J. Chen (2016), Fluid–rock interactions in seismic faults: Implications from the structures and mineralogical and geochemical compositions of drilling cores from the rupture of the 2008 Wenchuan earthquake, China, *Tectonophysics*, 666, 260–280, doi: 10.1016/j.tecto.2015.11.008.
- Ehlig, P. L. (1973), History, seismicity and engineering geology of the san gabriel fault, in *Geology, seismicity, and environmental impact*, pp. 247–251, Association of Engineering Geologist.
- Evans, J. P. (1990), Textures, deformation mechanisms, and the role of fluids in the cataclastic deformation of granitic rocks, in *Deformation Mechanisms, Rheology, and Tectonics*, pp. 29–39, Geological Society, London, Special Publications 54, doi: 10.1144/GSL.SP.1990.054.01.03.
- Evans, J. P., and F. M. Chester (1995), Fluid-rock interaction in faults of the San Andreas system: Inferences from San Gabriel fault rock geochemistry and microstructures, *Journal of Geophysical Research*, 100(B7), 13,007–13,020, doi: 10.1029/94jb02625.
- Evans, J. P., K. Crouch, C. Studnicki, S. Bone, N. Edwards, and S. Webb (2023), Fluid-rock interactions, hydrothermal processes, and accommodation of slip in shallow parts of the San Andreas and San Gabriel Faults, southern California, doi: 10.31223/X5X096.
- Faulkner, D. R., A. C. Lewis, and E. H. Rutter (2003), On the internal structure and mechanics of large strike-slip fault zones: field observations of the Carboneras fault in southeastern Spain, *Tectonophysics*, 367(3), 235–251, doi: 10.1016/S0040-1951(03)00134-3.
- Ferrill, D. A., A. P. Morris, M. A. Evans, M. Burkhard, R. H. Groshong, and C. M. Onasch (2004), Calcite twin morphology: a low-temperature deformation geothermometer, *Journal of Structural Geology*, 26(8), 1521–1529, doi: 10.1016/j.jsg.2003.11.028.
- Forand, D., J. P. Evans, S. U. Janecke, and J. Jacobs (2018), Insights into fault processes and the geometry of the San Andreas fault system: Analysis of core from the deep drill hole at Cajon Pass, California, *GSA Bulletin*, 130(1-2), 64–92, doi: 10.1130/B31681.1.
- Gratier, J.-P., P. Favreau, and F. Renard (2003), Modeling fluid transfer along California faults when integrating pressure solution crack sealing and compaction processes, *Journal of Geophysical Research*, 108, 2104, doi: 10.1029/2001JB000380.
- Haines, S. H., B. A. van der Pluijm, M. Ikari, D. Saffer, and C. Marone (2009), Clay fabric intensity in natural and artificial fault gouges: Implications for brittle fault zone processes and sedimentary basin clay fabric evolution, *Journal of Geophysical Research*, 114, B05,406, doi: 10.1029/2008JB005866.
- Hauksson, E., and M.-A. Meier (2019), Applying Depth Distribution of Seismicity to Determine Thermo-Mechanical Properties of the Seismogenic Crust in Southern California: Comparing Lithotectonic Blocks, *Pure and Applied Geophysics*, 176(3), 1061–1081, doi: 10.1007/s00024-018-1981-z.
- Holdsworth, R. E., E. W. E. van Diggelen, C. J. Spiers, J. H. P. de Bresser, R. J. Walker, and L. Bowen (2011), Fault rocks from the SAFOD core samples: Implications for weakening at shallow depths along the San Andreas Fault, California, *Journal of Structural Geology*, 33(2), 132–144, doi: 10.1016/j.jsg.2010.11.010.
- HSR (2019), Palmdale to Burbank Project Section, Preliminary Geotechnical Data Report for Tunnel Feasibility, Angeles National Forest, *Tech. rep.*, California High-Speed Rail Authority.
- Huang, Y., J.-P. Ampuero, and D. V. Helmberger (2014), Earthquake ruptures modulated by waves in damaged fault zones, *Journal of Geophysical Research, [Solid Earth]*, 119(4), 3133–3154, doi: 10.1002/2013jb010724.



- Ishikawa, T., M. Tanimizu, K. Nagaishi, J. Matsuoka, O. Tadai, M. Sakaguchi, T. Hirono, T. Mishima, W. Tanikawa, W. Lin, H. Kikuta, W. Soh, and S.-R. Song (2008), Coseismic fluid-rock interactions at high temperatures in the Chelungpu fault, *Nature Geoscience*, 1(10), 679–683, doi: 10.1038/ngeo308.
- Ishikawa, T., T. Hirono, N. Matsuta, K. Kawamoto, K. Fujimoto, J. Kameda, Y. Nishio, Y. Maekawa, and G. Honda (2014), Geochemical and mineralogical characteristics of fault gouge in the Median Tectonic Line, Japan: evidence for earthquake slip, *Earth, Planets and Space*, 66(1), 1–20, doi: 10.1186/1880-5981-66-36.
- Jefferies, S. P., R. E. Holdsworth, C. A. J. Wibberley, T. Shimamoto, C. J. Spiers, A. R. Niemeijer, and G. E. Lloyd (2006), The nature and importance of phyllonite development in crustal-scale fault cores: an example from the Median Tectonic Line, Japan, *Journal of Structural Geology*, 28(2), 220–235, doi: 10.1016/j.jsg.2005.10.008.
- Jennings, C. W., and R. G. Strand (1969), Los Angeles Geologic Map, 1:250,000.
- Kaneko, Y., and Y. Fialko (2011), Shallow slip deficit due to large strike-slip earthquakes in dynamic rupture simulations with elasto-plastic off-fault response, *Geophysical Journal International*, 186(3), 1389–1403, doi: 10.1111/j.1365-246X.2011.05117.x.
- Lee, H. K., and H. P. Schwarcz (1996), Electron spin resonance plateau dating of periodicity of activity on the San Gabriel fault zone, southern California, *Geological Society of America bulletin*, 108, 735–746.
- Marchandon, M., J. Hollingsworth, and M. Radiguet (2021), Origin of the shallow slip deficit on a strike slip fault: Influence of elastic structure, topography, data coverage, and noise, *Earth and Planetary Science Letters*, 554, 116,696, doi: 10.1016/j.epsl.2020.116696.
- Marone, C., and D. M. Saffer (2007), 12. Fault Friction and the Upper Transition from Seismic to Aseismic Faulting, in *The Seismogenic Zone of Subduction Thrust Faults*, edited by T. H. Dixon and J. C. Moore, pp. 346–369, Columbia University Press, doi: 10.7312/dixo13866-012.
- Mitchell, T. M., and D. R. Faulkner (2009), The nature and origin of off-fault damage surrounding strike-slip fault zones with a wide range of displacements: A field study from the Atacama fault system, northern Chile, *Journal of Structural Geology*, 31(8), 802–816, doi: 10.1016/j.jsg.2009.05.002.
- Nevitt, J. M., B. A. Brooks, R. D. Catchings, M. R. Goldman, T. L. Erickson, and C. L. Glennie (2020), Mechanics of near-field deformation during co- and post-seismic shallow fault slip, *Scientific Reports*, 10(1), 5031, doi: 10.1038/s41598-020-61400-9.
- Nourse, J. A. (2002), Middle Miocene reconstruction of the central and eastern San Gabriel Mountains, southern California, with implications for evolution of the San Gabriel fault and Los Angeles basin, *Geological Society of America Special Paper*, 365, 161–185, doi: 10.1130/0-8137-2365-5.161.
- Ohtani, T., K. Fujimoto, H. Ito, H. Tanaka, N. Tomida, and T. Higuchi (2000), Fault rocks and past to recent fluid characteristics from the borehole survey of the Nojima fault ruptured in the 1995 Kobe earthquake, southwest Japan, *Journal of Geophysical Research*, 105(B7), 16,161–16,171, doi: 10.1029/2000jb900086.
- Powell, R. E. (1993), Chapter 1: Balanced palinspastic reconstruction of pre-late Cenozoic paleogeology, southern California: Geologic and kinematic constraints on evolution of the San Andreas fault system, in *Geological Society of America Memoirs*, edited by R. E. Powell and E. al., Memoir - Geological Society of America, pp. 1–106, Geological Society of America, doi: 10.1130/mem178-p1.
- Roten, D., K. B. Olsen, and S. M. Day (2017a), Off-fault deformations and shallow slip deficit from dynamic rupture simulations with fault zone plasticity, *Geophysical Research Letters*, 44(15), 7733–7742, doi: 10.1002/2017gl074323.
- Roten, D., K. B. Olsen, S. M. Day, and Y. Cui (2017b), Quantification of fault-zone plasticity effects with spontaneous rupture simulations, *Pure and Applied Geophysics*, 174, 3369–3391, doi: 10.1007/s00024-017-1466-6.
- Rowe, K. J., and E. H. Rutter (1990), Palaeostress estimation using calcite twinning: experimental calibration and application to nature, *Journal of Structural Geology*, 12(1), 1–17, doi: 10.1016/0191-8141(90)90044-Y.
- Rutter, E. H. (1986), On the nomenclature of the mode of failure, transitions in rocks, *Tectonophysics*, 122, 381–387.
- Rutter, E. H., D. R. Faulkner, and R. Burgess (2012), Structure and geological history of the Carboneras Fault Zone, SE Spain: Part of a stretching transform fault system, *Journal of Structural Geology*, 45, 68–86, doi: 10.1016/j.jsg.2012.08.009.
- Schleicher, A. M., S. N. Tourscher, B. A. van der Pluijm, and L. N. Warr (2009), Constraints on mineralization, fluid-rock interaction, and mass transfer during faulting at 2–3 km depth from the SAFOD drill hole, *Journal of Geophysical Research, [Solid Earth]*, 114(B04202), doi: 10.1029/2008JB006092.
- Schleicher, A. M., B. A. van der Pluijm, and L. N. Warr (2012), Chlorite-smectite clay minerals and fault behavior: New evidence from the San Andreas Fault Observatory at Depth (SAFOD) core, *Lithosphere*, 4(3), 209–220, doi: 10.1130/L158.1.
- Scholz, C. H. (1988), The brittle-plastic transition and the depth of seismic faulting, *Geologische Rundschau: Zeitschrift für allgemeine Geologie*, 77(1), 319–328, doi: 10.1007/BF01848693.
- Scholz, C. H. (2019), *The Mechanics of Earthquakes and Faulting*, 3rd ed., 493 pp., Cambridge University Press.
- Schulz, S. E., and J. P. Evans (1998), Spatial variability in microscopic deformation and composition of the Punchbowl fault, southern California: implications for mechanisms, fluid-rock interaction, and fault morphology, *Tectonophysics*, 295(1), 223–244, doi: 10.1016/S0040-1951(98)00122-X.
- Schulz, S. E., and J. P. Evans (2000), Mesoscopic structure of the Punchbowl Fault, Southern California and the geologic and geophysical structure of active strike-slip faults, *Journal of Structural Geology*, 22(7), 913–930, doi: 10.1016/S0191-8141(00)00019-5.
- Scott, C., J. Champenois, Y. Klinger, E. Nissen, T. Maruyama, T. Chiba, and R. Arrowsmith (2019), The 2016 M7 Kumamoto, Japan, earthquake slip field derived from a joint inversion of differential lidar topography, optical correlation, and InSAR surface displacements, *Geophysical Research Letters*, 46, 6341–6351, doi: 10.1029/2019GL083785.
- Shinevar, W. J., M. D. Behn, G. Hirth, and O. Jagoutz

- (2018), Inferring crustal viscosity from seismic velocity: Application to the lower crust of Southern California, *Earth and Planetary Science Letters*, 494, 83–91, doi: 10.1016/j.epsl.2018.04.055.
- Sibson, R. H. (1977), Fault rocks and fault mechanisms, <https://www.lyellcollection.org/doi/10.1144/gsjgs.133.3.0191>, doi: 10.1144/gsjgs.133.3.0191, accessed: 2023-9-15.
- Song, S.-R., L.-W. Kuo, E.-C. Yeh, C.-Y. Wang, J.-H. Hung, and K.-F. Ma (2007), Characteristics of the lithology, fault-related rocks and fault zone structures in TCDP hole-A, *TAO: Terrestrial, Atmospheric and Oceanic Sciences*, 18(2), 243, doi: 10.3319/tao.2007.18.2.243(tcdp).
- Studnický, C. (2021), Constraining Deformation Mechanisms of Fault Damage Zones: A Case Study of the Shallow San Andreas Fault at Elizabeth Lake, Southern California, Master's thesis, Utah State University, doi: 10.26076/638e-3616.
- Sutherland, R., V. G. Toy, J. Townend, S. C. Cox, J. D. Eccles, D. R. Faulkner, D. J. Prior, R. J. Norris, E. Mariani, C. Boulton, B. M. Carpenter, C. D. Menzies, T. A. Little, M. Hasting, G. P. De Pascale, R. M. Langridge, H. R. Scott, Z. Reid Lindroos, B. Fleming, and A. J. Kopf (2012), Drilling reveals fluid control on architecture and rupture of the Alpine fault, New Zealand, *Geology*, 40(12), 1143–1146, doi: 10.1130/G33614.1.
- Thakur, P., Y. Huang, and Y. Kaneko (2020), Effects of low-velocity fault damage zones on long-term earthquake behaviors on mature strike-slip faults, *Journal of Geophysical Research, [Solid Earth]*, 125(8), e2020JB019587, doi: 10.1029/2020jb019587.
- Wang, K. (2021), If Not Brittle: Ductile, Plastic, or Viscous?, *Seismological Research Letters*, 92(2A), 1181–1184, doi: 10.1785/0220200242.
- Warr, L. N., and S. S. Cox (2001), Clay mineral transformations and weakening mechanisms along the Alpine Fault, New Zealand, <https://www.lyellcollection.org/doi/10.1144/GSL.SP.2001.186.01.06>, doi: 10.1144/GSL.SP.2001.186.01.06, accessed: 2023-9-15.
- Weber, F. H. (1982), Geology and geomorphology along the San Gabriel fault zone, Los Angeles and Ventura counties, California, *Tech. rep.*, Div. Mines and Geology Open File Report.
- Wibberley, C. A. J., and T. Shimamoto (2003), Internal structure and permeability of major strike-slip fault zones: the Median Tectonic Line in Mie Prefecture, Southwest Japan, *Journal of Structural Geology*, 25(1), 59–78, doi: 10.1016/S0191-8141(02)00014-7.
- Wibberley, C. A. J., G. Yielding, and G. Di Toro (2008), Recent advances in the understanding of fault zone internal structure; a review, *Structure of Fault Zones: Implications for Mechanical and Fluid-flow Properties, Geological Society of London Special Publication*, 299, 5–33, doi: 10.1144/SP299.2 0305-8719/08.
- Williams, C. F., and J. DeAngelo (2011), Evaluation of approaches and associated uncertainties in the estimation of temperatures in the upper crust of the Western United States, *GRC Transactions*, 35, 1599–1605.
- Williams, R. T., C. D. Rowe, K. Okamoto, H. M. Savage, and E. Eves (2021), How fault rocks form and evolve in the shallow San Andreas fault, *Geochemistry, Geophysics, Geosystems*, 22(11), e2021GC010092, doi: 10.1029/2021gc010092.
- Woodcock, N. H., and K. Mort (2008), Classification of fault breccias and related fault rocks, *Geological Magazine*, 145(3), 435–440, doi: 10.1017/S0016756808004883.
- Yeats, R. S., G. J. Huftile, and L. T. Stitt (1994), Late Cenozoic Tectonics of the East Ventura Basin, Transverse Ranges, California, *AAPG Bulletin*, 78(7), 1040–1074, doi: 10.1306/A25FE42D-171B-11D7-8645000102C1865D.
- Yerkes, R. F., and R. H. Campbell (2005), Preliminary Geologic Map of the Los Angeles 30' x 60' Quadrangle, Southern California, version 2.1, 1:100000 scale, *U. S. Geological Survey Open-file Report*.
- Zoback, M., S. Hickman, and W. Ellsworth (2010), Scientific drilling into the San Andreas fault zone, *Eos*, 91(22), 197–199, doi: 10.1029/2010eo220001.